Local chromatin context dictates the genetic determinants of the heterochromatin spreading reaction.

R.A. Greenstein[1,2,†], Henry Ng[1,2,†], Ramon R. Barrales[3,#], Catherine Tan[5,6], Sigurd Braun[3,4], and Bassem Al-Sady[1,*]

[1]Department of Microbiology &Immunology, George Williams Hooper Foundation, University of California San Francisco, San Francisco, CA 94143, USA, [2]TETRAD graduate program, University of California San Francisco, San Francisco, CA 94143, USA, [3], Biomedical Center, Department of Physiological Chemistry, Ludwig-Maximilians-University of Munich, Planegg-Martinsried, Germany, [4]International Max Planck Research School for Molecular and Cellular Life Sciences, Martinsried, Germany, [#]current address: Centro Andaluz de Biología del Desarrollo, Universidad Pablo de Olavide de Sevilla-Consejo Superior de Investigaciones Científicas-Junta de Andalucía, Sevilla, Spain. [5]Department of Cell and Tissue Biology, University of California San Francisco, San Francisco, CA 94143, USA, [6]Biomedical Sciences graduate program, University of California San Francisco, San Francisco, CA 94143, USA

† these authors contributed equally to this work.

[*]correspondence: bassem.al-sady@ucsf.edu

Abstract

Heterochromatin spreading, the expansion of gene-silencing structures from DNA-encoded nucleation sites, occurs in distinct chromatin contexts. Spreading re-establishes gene-poor constitutive heterochromatin every cell cycle, but also invades gene-rich euchromatin *de novo* to steer fate decisions. Unlike heterochromatin nucleation and assembly, the determinants of the spreading process remain poorly understood. Our heterochromatin spreading sensor separately records nucleation site-proximal, and distal, heterochromatin gene silencing. By screening a nuclear function gene deletion library in fission yeast, we identified regulators that alter the propensity, both positively and negatively, of a nucleation site to spread heterochromatin. Critically, the involvement of many regulators is conditioned by the chromatin context within which spreading occurs. We find spreading, but not nucleation, within constitutive heterochromatin, requires distinct Clr6 histone deacetylase complexes. However, spreading is universally antagonized by a suite of chromatin remodelers. Our results disentangle the machineries that control lateral heterochromatin spreading from those that instruct DNA-directed assembly.

Introduction

Cellular specification requires the genome to be partitioned into regions of activity and inactivity such that only genes appropriate for a given cellular state are available for expression. This requires the formation and propagation, in time and space, of gene-repressive heterochromatin structures. Heterochromatin is most commonly seeded by DNA-directed nucleation (Hall et al. 2002; Reyes-Turcu et al. 2011), and then propagates across the chromosome by a DNA-sequence indifferent process termed spreading, to repress genes expression in the underlying regions. Silencing is instructed by assembly factors, such as HP1, that recognize heterochromatic chemical modifications (Jacobs et al. 2001; Lachner et al. 2001). The spreading of silencing structures occurs in very different chromatin contexts, which may intrinsically promote or antagonize this process: (1) Constitutive heterochromatin, which is generally gene-poor and as such depleted of activities associated with active genes known to antagonize heterochromatin (Scott et al. 2006; Greenstein et al. 2019). Its maintenance through replication is aided by the inheritance of nucleosomes bearing heterochromatic marks (Alabert et al. 2015). This inheritance promotes modification of nearby nucleosomes due to the "read-write" positive feedback intrinsic to heterochromatin histone modifiers (Zhang et al. 2008; Al-Sady et al. 2013; Ragunathan et al. 2015). (2) Conversely, during differentiation, heterochromatin is either seeded at new nucleation sites or invades gene-rich euchromatin *de-novo* from existing nucleation sites (Wen et al. 2009; Zhu et al. 2013; Zylicz et al. 2015; Zylicz et al. 2018; Nicetto and Zaret 2019). In either case, it encounters active chromatin that lacks repressive marks and can specifically antagonize heterochromatin (Greenstein et al. 2019). Thus, during this initial invasion process, heterochromatin spreading cannot benefit from the inheritance through replication of pre-existing marked nucleosomes. Beyond the differences between active and inactive chromatin, it remains unclear whether distinct nucleation elements require different regulators

23 to enact efficient spreading outward from those sites. Nonetheless, we recently described that distinct
24 nucleation elements trigger divergent types of spreading behavior (Greenstein et al. 2018).

25 Over the past four decades, forward and reverse genetic screens in fission yeast have established
26 an exhaustive list of factors required for heterochromatin silencing and heterochromatin nucleation.
27 Some of these nucleation mechanisms include repeat sequences that instruct specialized RNAi-
28 machinery to process noncoding (nc) RNAs involved in targeting the histone methyl transferase Clr4
29 (Moazed 2009); signals within nascent transcripts that trigger heterochromatin island formation (Zofall
30 et al. 2012); and shelterin-dependent pathways (Wang et al. 2016; Zofall et al. 2016). However, those
31 genetic screens have neither directly addressed factors that specifically regulate the spreading process,
32 nor whether such factors act in general or context-specific settings. With our previously established
33 fluorescent reporter-based heterochromatin spreading sensor (HSS) we can segregate the central output
34 of heterochromatin (gene silencing) from the spatial control of the reaction (spreading) (Greenstein et al.
35 2018; Greenstein et al. 2019). This allows us to address the following questions: (1) Are there known or
36 novel regulators of heterochromatin that primarily regulate spreading, versus nucleation? (2) Does
37 spreading over chromatin with distinct characteristics, such as gene density or nucleosome arrangement,
38 require different sets of regulators? (3) Does the set of regulators required for efficient spreading depend
39 on the type of nucleator that seeds it - for example nucleators using transcription and ncRNA pathways
40 versus direct tethering of heterochromatic factors?

41 To address these questions, we conducted a series of reverse genetic screens in fission yeast,
42 using a custom nuclear function gene deletion library in four heterochromatin contexts. These include
43 derivations of the fission yeast mating type (MAT) locus, a gene-poor constitutive heterochromatin
44 region contained by *IR-L* and *IR-R* boundaries and nucleated by at least two elements: (1) *cenH,*
45 homologous to pericentromeric *dh* and *dg* elements, which rely on ncRNA pathways, including RNAi,

46 and (2) *REIII*, a sequence element that directly recruits heterochromatin factors via the stress-response
47 transcription factors Atf1 and Pcr1 (Jia et al. 2004; Kim et al. 2004). We also queried an ectopic
48 heterochromatin domain that is embedded in gene rich euchromatin. This domain is nucleated by an
49 ectopically inserted *dh* element fragment proximal to the *ura4* locus (Canzio et al. 2013; Marina et al.
50 2013; Greenstein et al. 2018).

51 We find that the genetic requirements for promotion and containment of heterochromatin
52 spreading diverge significantly between different chromatin contexts, and to some degree also between
53 different types of nucleators. However, despite these context-dependent differences for spreading,
54 common themes also emerge from this work: (1) Sub-complexes of the Clr6 histone deacetylase
55 (HDAC) complex, in particular the Fkh2-associated Clr6 complex I″, appear to promote spreading, but
56 not nucleation, at multiple heterochromatin loci. (2) At both euchromatic and heterochromatic loci,
57 spreading is antagonized by a diverse set of nucleosome remodelers, in particular Ino80 and Swr1C. (3)
58 Unexpectedly, members of an AP3 adaptor complex, normally involved in membrane traffic, are
59 moderate positive regulators of spreading in hetero- and euchromatin. Together, these results
60 specifically pinpoint the machineries required to regulate the spatial expansion of heterochromatin
61 domains independent of the initial seeding by DNA-encoded nucleation sites.

62 **Results**

63 Our previously developed HSS relies on three transcriptionally-encoded fluorescent protein-
64 coding genes that collectively report single cell measurements of heterochromatin formation via flow
65 cytometry, while normalizing for transcriptional and translational noise (Al-Sady et al. 2016; Greenstein
66 et al. 2018). It provides separate, quantitative recordings of nucleation-proximal ("green") and distal
67 ("orange") events at a heterochromatin site over large populations of isogenic cells (typically N
68 >20,000) (**Figure 1A**). In contrast to the singular readout employed by auxotrophy-dependent reporter

69 gene silencing assays, the HSS assay provides a "multidimensional snapshot" that distinguishes changes
70 in heterochromatin nucleation and spreading, and additionally permits tracking of emerging multimodal
71 cell populations and unique population distributions. This is an important conceptual advance compared
72 to traditional methods.

73 With this ability to observe the entire population distribution pattern from any isogenic
74 background, we sought first to investigate the requirements for heterochromatin activity for both
75 nucleation and distal spreading, within either constitutive heterochromatin or gene-rich euchromatic
76 regions. Further, we queried whether different types of heterochromatic nucleation sequences utilize
77 similar or different sets of regulators to nucleate and/or spread the resulting heterochromatin structures
78 outwards. To address the latter, we explored three different chromatin contexts, derived from the
79 constitutive heterochromatic mating type (MAT) locus, each containing an embedded HSS (**Figure 1A**)
80 (Greenstein et al. 2018): wild type, with the *cenH* and *REIII* nucleating DNA elements uncompromised,
81 and two *MAT* variants that contained mutations in either the *cenH* or *REIII* elements (**Figure 1A**).
82 Mutations in these DNA elements limit initiation of heterochromatin spreading to one nucleator
83 (Greenstein 2018). To address differences in chromatin context in addition to variants of the constitutive
84 MAT locus, we examined heterochromatin formation at the euchromatic *ura4* locus, where
85 heterochromatin spreading is ectopically driven by the upstream insertion of a pericentromeric *dh* DNA
86 element (Marina et al. 2013; Greenstein et al. 2018). We refer to this chromatin context as *ECT*
87 (ectopic). When analyzed by flow cytometry, *WT MAT* and *MAT ΔcenH* populations appear largely
88 fully nucleated with near-complete local spreading, as evidenced by population density in the bottom
89 left in the 2D density histogram (**Figure 1C**,**D** (Greenstein et al. 2018)). *MAT ΔREIII* and *ECT* cell
90 populations, while mostly nucleated, display a stochastic distribution of spreading states, evidenced by a
91 vertical distribution on the left of the 2D density histogram (**Figure 1E,F** (Greenstein et al. 2018)). The

92 distribution of cells in a strong loss of silencing mutant, *Δclr3,* is shown for all chromatin contexts next
93 to the wild-type parents (**Figure 1C-F**). To identify potential regulators of the spreading reaction, we
94 conducted a genetic screen by crossing a deletion library of ~400 nuclear function genes (**Table 1**,
95 **Figure 1 Supplement 1**) to reporter strains with the HSS integrated in the four chromatin contexts
96 described above. We quantified the fluorescence signal from the three reporters in each mutant by flow
97 cytometry, with approximately 20k-30k cells per mutant, depending on growth conditions.

98 To visualize the pattern of heterochromatin domain activity across the isogenic mutant
99 populations, we first employed t-distributed stochastic neighbor embedding (t-SNE). For all the mutants
100 in each chromatin context, we converted the normalized 2D distribution of cells into a numerical vector
101 representing cell density in 25 isometric plot regions as different parameters (**Figure 1B**). The t-SNE
102 model was built by calculating the similarity between different cell distributions and comparing these 25
103 parameters from all mutants and wild type controls in the four chromatin contexts (**Figure 1B**).

104 We plotted the t-SNE model with all the four chromatin contexts and respective mutants,
105 coloring each mutant by its parental chromatin context (**Figure 1G**). We also colored the mutants by the
106 median nucleation ("green", **Figure 1H**) or spreading ("orange", **Figure 1I**) reporter expression values.
107 As expected, the majority of mutants did not strongly deviate from their parent and broadly clustered
108 together into a "neighborhood" by chromatin context. This is evident for *ECT*, for which the parent
109 strain has "green" and "orange" in a less repressed state, particularly compared to *WT MAT* and *MAT*
110 *ΔcenH.* Within each neighborhood, the distribution of "orange" expression, especially for *MAT ΔREIII*
111 and *ECT*, is graded from above to below the expression level of the parent(s), revealing a continuum of
112 mutants with enhanced or abrogated spreading. We could not find mutants that display more repression
113 than the parental strains of *MAT ΔcenH,* which are highly repressed in the OFF state, as previously
114 described (Grewal and Klar 1996; Greenstein et al. 2018). However, we did observe mutants located

115 out of the area of their chromatin context-driven "neighborhood". First, the major known
116 heterochromatin mutants, *Δclr4, Δswi6, Δclr3* among others, from each chromatin context formed a
117 cluster with high expression of "green" and "orange" (**Figure 1I** enlarged region, exemplified by *Δclr3*),
118 segregating from the rest of the population. Second, we observed mutants, such as *Δcdt2, Δepe1* and
119 *Δchp1,* that segregate out of neighborhood only for selected chromatin contexts, indicating specificity
120 (highlighted in **Figure 1I**). The t-SNE analysis visualized the relationship of all four chromatin contexts,
121 and mutants therein, with respect to their nucleation and spreading behavior, directly revealing the
122 graded nature of mutant phenotypes. This is particularly the case with respect to spreading in *ECT* and
123 *MAT ΔREIII* neighborhoods (**Figure 1I**)

124 However, in the t-SNE analysis the phenotype patterns are weighted by the intrinsic behavior of
125 each parent's chromatin context. To quantify how much each mutation impacted the heterochromatin
126 state in each chromatin context, we performed Earth Mover's Distance analysis (EMD, **Figure 1J** see
127 also materials and methods and (Orlova et al. 2016)). We express the contribution of each mutant
128 relative to the parental isolates by a quotient of their respective EMDs to *Δclr4*, which is completely
129 deficient in heterochromatin assembly and serves as a fixed reference point for all chromatin contexts.
130 We represent a subset of the mutants' EMD values in a heatmap (**Figure 1K**). Some mutants contributed
131 similarly in different chromatin contexts, such as *Δclr3* and *Δrik1,* which display strong de-repression,
132 and *Δair1,* which displays an intermediate de-repression (Thon et al. 1999; Keller et al. 2010). However,
133 many mutants had differential contributions in each chromatin context. As an example, *Δpob3,* a
134 mutation in the FACT complex (Lejeune et al. 2007), had weaker phenotypes where nucleation is solely
135 ncRNA-driven (*MAT ΔREIII* and *ECT*) and stronger phenotypes when *REIII,* an ncRNA-independent
136 element, is intact (*WT MAT* and *MAT ΔcenH*) (**Figure 1K**). Interestingly, the TRAMP subunit mutant
137 *Δcid14*, had more pronounced roles in *MAT* contexts over *ECT* (**Figure 1K**). Beyond these more subtle

138 differences, we noticed a large divergence between *ECT* and other contexts. This is evident from very
139 low pairwise correlations of $EMD^{mut/par}$ values between all the mutants for *ECT* against the *MAT*
140 contexts (**Figure 1, Supplement 2 C,E,F**). Conversely, we observe much higher correlations between
141 all pairwise combinations of the three *MAT* chromatin contexts (**Figure 1, Supplement 2 A,B,D**). The
142 divergence between *MAT* and *ECT* contexts is especially true for the RNAi pathway. *Δchp1* and *Δtas3*
143 (members of RITS complex), *Δdsh1* (RNAi factor), *Δcid12* (member of RDRC complex), and *Δsaf1*
144 (RNAi associated splicing factor (Bayne et al. 2014)) all have very strong effects only in *ECT*.

145 The above results are consistent with previous reports of *WT MAT* and ectopic reporters (Hall et
146 al. 2002), which are respectively independent and dependent on RNAi for heterochromatin maintenance.
147 Surprisingly, *MAT ΔREIII,* which similar to *ECT* solely relies on a *dh*-homologous *cenH* element for
148 H3K9me nucleation, also behaved independent of RITS for maintenance (**Figure 1K**). *MAT* has another
149 H3K9me-independent silencing element, *REII* (Hansen et al. 2011), which is located upstream of
150 "green". However, this element appears to act quite locally (Ayoub et al. 2000; Hansen et al. 2011).
151 Moreover, we showed removal of *REII* had no effect on expression of HSS reporters in *MAT ΔcenH*
152 (Greenstein et al. 2018). Thus, we do not believe *REII* accounts for the difference observed between
153 *MAT ΔREIII* and *ECT*.

154 Similar to RNAi factors, the heterochromatin-antagonizing *epe1* pathway had strikingly different
155 impacts on the *MAT* chromatin contexts compared to *ECT* (**Figure 1G**). *Δepe1* results in destabilized
156 heterochromatin at *ECT,* but the deletion has little effect at *MAT* chromatin contexts. Heterochromatin in
157 these contexts instead is sensitive to mutations in the Epe1-turnover pathway, exemplified by *cdt2*, the
158 specificity factor for the Epe1-targeting E3 ubiquitin ligase (Braun et al. 2011). In contrast to loss of
159 silencing mutants, we also identified mutations that induce hyper-repressed states ($EMD^{mut/par}$ >1) in

160 multiple chromatin contexts with some differences in contribution to hyper-repression. These included
161 *Δyap9, Δsnf22, Δswc5* and *Δiec3* (see below).

162 Overall, the EMD analysis enabled us to systematically and quantitatively discern how each
163 mutant contributes to the combined nucleation and spreading heterochromatin state within each
164 chromatin context. The results suggest that the genetic circuitry for heterochromatin maintenance differs
165 significantly between naïve sites in euchromatin and constitutive loci. This is consistent with the tightly
166 repressed *MAT ΔcenH* or the redundantly nucleated *WT MAT.* But the fact that *MAT ΔREIII* also
167 diverged strongly from *ECT* in its dependence on genes for heterochromatin nucleation and spreading
168 was more surprising, because both contexts are driven exclusively by a similar ncRNA nucleators, *cenH*
169 and *dh* (Hansen et al. 2006), and display stochastic spreading over similar ranges (**Figure 1C, F**).
170 Further we previously showed that they both exhibit dynamically unstable heterochromatin over time
171 (Greenstein et al. 2018). The finding that even heterochromatin domains with very similar nucleation
172 and spreading dynamics rely on different regulators for their maintenance, suggests that such context-
173 specific requirements for heterochromatin assembly are likely common across the genome.

174 The above analyses addressed the genetic requirements for heterochromatin silencing, including
175 both nucleation and distal spreading, in different chromatin contexts. Next, we aimed to identify
176 regulators that are specific to heterochromatin spreading but function independent of nucleation. To do
177 so, we employed the capability of the HSS to segregate those activities. We isolated cell populations that
178 reside within a "green"-off gate which represents cells with heterochromatin fully assembled at the
179 nucleation site (see methods, and (Greenstein et al. 2018)). To quantify increased or decreased spreading
180 in a given mutant, we calculated a $Grid_n^{mut/par}$ metric (described in Methods), which tracks the changes
181 of cell distributions in "orange" expression within the "green"-off gate (**Figure 2A**). To isolate gain or
182 loss of spreading mutants (hits) for further analysis, we only considered the top 15% of mutants in which

183 $Grid_n^{mut/par}$ values were also above 2 standard deviations from the mean of the replicate parent isolates.
184 (**Figure 2 Supplement 1**). With these gene hits isolated, we proceeded to analyze their relationships
185 within and across chromatin contexts.

186 We first examined the degree to which spreading modulators are shared between chromatin
187 contexts via upset plots (**Figure 2B&C**). Conceptually similar to a Venn diagram, this analysis allows
188 rapid visualization of the degree of overlap between sets, with the number of shared genes plotted as a
189 bar graph and the sets each bar represents annotated below the plot. The upset plot for loss of spreading
190 phenotypes (*i.e.* genes that promote spreading, **Figure 2B**) showed that exceedingly few genes, three out
191 of 164 unique genes found as hits, are shared across all chromatin contexts (*csn1, rrp17, apm3*). This
192 result emphasizes the specific impact that each chromatin context has on heterochromatin spreading.
193 Seven genes were shared across all the MAT locus chromatin contexts. In contrast, 111 genes
194 contributed only to one chromatin context. The degree to which genes contributed positively towards
195 spreading, and the degree of overlap across chromatin contexts is shown in bar-graphs of $Grid_n^{mut/par}$ in
196 **Figure 2D-G**. We additionally show the 2D density histogram of the screen mutants for the top two loss
197 of spreading hits for each chromatin context in **Figure 2H-K**. The top two hits for *MAT ΔcenH* were
198 *gad8* and *cdt2* (**Figure 2E&I**) The significant contribution of *cdt2* suggests that Epe1specifically limits
199 spreading in *MAT ΔcenH* compared to other chromatin contexts. Spreading in *WT MAT* and *MATΔREIII*
200 was most dependent on *fkh2,* while the second strongest hits were *rrp6* and *prw1,* respectively (**Figure**
201 **2D,F,H,J** and see below). Prw1 and Fkh2 form parts of Clr6 complexes (see below), while Rrp6 is a
202 central part of the exosome, required for gene silencing in multiple ncRNA-dependent pathways (Buhler
203 et al. 2007). The top hit in *ECT* was the Csn1 COP9 signalosome subunit, which has been implicated in
204 neddylation of cullin-based E3 ligases and may operate in a similar pathway as Cdt2 (Bayne et al. 2014).

205 *ECT* was also highly sensitive to *Δpht1* (**Figure 2G**) which codes for H2A.Z, normally associated with
206 antagonizing spreading (Meneghini et al. 2003).

207 We also observed a significant number of genes that showed gain of spreading in *WT MAT, MAT*
208 *ΔREIII* and *ECT* (**Figure 2C)**. We could not examine *MAT ΔcenH* for this phenotype because this
209 chromatin context is highly repressed in the OFF state as reported previously (Grewal and Klar 1996;
210 Greenstein et al. 2018). Six out of 98 genes found as hits are shared across these three chromatin
211 contexts (**Figure 2C**, **Figure 2 Supplement 2**). The 2D density histograms of the screen mutants are
212 shown for top two hits per chromatin context (**Figure 2 Supplement 2D-F)**. Validating the approach,
213 we found *leo1,* a gene previously impacted in spreading control across boundaries (Verrier et al. 2015),
214 as a moderate gain of spreading hit. *ECT* displayed the largest fraction, 43 out of 58 of spreading-
215 antagonizing genes that are unique to one context. In contrast, we found 11 out of 43 genes unique to
216 *MAT ΔREIII*, which displays a very similar spatio-temporal spreading behavior to *ECT.* This likely
217 reflects that even though heterochromatin can assemble in a euchromatin context, spreading is under
218 multiple layers of constraint in this setting.

219 To understand which nuclear pathways, as opposed to individual genes, direct or antagonize
220 heterochromatin spreading across backgrounds, we performed a protein complex-level analysis. Using
221 the Gene Ontology (GO) protein complex annotations from Pombase (Lock et al. 2018), we annotated
222 the GO complex membership of each screen hit and tabulated the frequency ("counts") of each GO
223 complex per background in both loss of spreading (loss) and gain of spreading (gain) categories. Using
224 these GO complex counts, we generated a heatmap for all the protein complexes represented by hits in
225 our screen (**Figure 3A**). In order to assess the similarities between chromatin contexts (*WT MAT, MAT*
226 *ΔcenH, MAT ΔREIII, ECT*) and categories (loss or gain of spreading) we performed unsupervised
227 clustering on the heatmap columns. Broadly, the hit categories (loss or gain of spreading) clustered

228 together, (**Figure 3A**, bottom), revealing relative similarity at the GO complex level. The exception
229 however was the *ECT* "loss" set of hits. Consistent with our gene-level analysis (**Figure 2B-G, Figure 2**
230 **Supplement 2**), complexes that contribute most strongly to "loss" and "gain" categories are different in
231 *ECT* compared to the *MAT* variants.

232 Overall, we identified three common trends within and between categories: (1) a role for
233 antagonizing spreading by chromatin remodelers, (2) a role of histone deacetylase complexes (HDACs),
234 in particular Clr6 sub-complexes, in promoting spreading, and (3) a role for a small number of additional
235 known and novel spreading regulators, including the AP-3 adaptor and COP9 signalosome complex,
236 which promoted spreading across all backgrounds.

237 As evidenced by the heatmap (**Figure 3A, top right**), chromatin remodeling complexes are
238 strongly represented in the gain of spreading hit category, including the Swr1C, Ino80, SWI/SNF, and
239 RSC-type complexes. To explore this further, we assessed which protein components were contributing
240 to these GO complex counts. For all the genes annotated to a given chromatin remodeling complex and
241 present in our screen, we displayed whether they were identified as a hit (blue) or not (grey) (**Figure**
242 **3B**). Indeed, we found that the large majority of the gene hits annotated fall within the "gain" category
243 across backgrounds. The manner in which the cell distributions change in these screen hits is evident
244 from the 2D density histograms (**Figure 3 Supplement 1)**. While complex-specific heterochromatin
245 antagonizing activities have previously been ascribed to chromatin remodelers, such as Swr1C
246 (Meneghini et al. 2003) and Ino80 (Xue et al. 2015), we observe a broad involvement across remodelers.
247 The specific contributions of these remodeling complexes to destabilizing heterochromatin spreading are
248 interesting candidates for future studies.
249

250 Most of the GO complexes we found to be required for spreading have been implicated in
251 chromatin regulation or silencing pathways specifically (**Figure 3A**). One notable exception was two
252 predicted subunits of the AP-3 adaptor complex, Apm3 and Apl5, with roles either in all chromatin
253 contexts (Apm3) or only in *MAT* contexts (Apl5). We were intrigued by the discovery of an AP-3
254 adaptor protein complex normally associated with vesicular traffic. While the spreading phenotype is
255 moderate, *apm3* is one of only three genes that display a loss of spreading phenotype across all contexts,
256 along with *csn1* and *rrp17* encoding a key member of the COP9 signalosome and a putative rRNA
257 exonuclease, respectively. Thus, we sought to examine whether this phenotype correlates with a
258 H3K9me2 spreading defect and assessed H3K9me2 levels at the constitutive and facultative
259 heterochromatin loci by chromatin immunoprecipitation followed by qPCR (ChIP-qPCR). Consistent
260 with its moderate phenotype, *Δapm3* had mildly reduced H3K9me2 within the MAT locus, but not at
261 pericentromeres and subtelomeres (**Figure 3, Supplement 2A-C**). Importantly we find a role for Apm3
262 in H3K9me2 accumulation at heterochromatin islands, including *mei4, ssn4* and *mcp7* (**Figure 3**
263 **Supplement 2D**), indicating a role in facultative heterochromatin. Since AP-3 adaptor proteins are
264 cytoplasmic, we tested whether a fraction of Apm3 and Apl5 is also targeted to the nucleus. We
265 expressed Apm3 and Apl5 as fusions with SF-GFP and visualized them together with Swi6:E2C, which
266 marks heterochromatin foci in the nucleus (**Figure 3 Supplement 2E**). Notably, we found that
267 Apm3:SF-GFP is distributed broadly in both the cytosol and nucleus, whereas the related Apl5 protein
268 appeared to be excluded from the nucleus (**Figure 3 Supplement 2F**). Together, these data indicate that
269 Apm3 may represent a novel regulator of heterochromatin spreading, which is also supported by the
270 finding that it physically interacts with the heterochromatin regulators Fft3 (Lee et al. 2017) and Epe1
271 (Wang et al. 2013).

272 The relationship between histone deacetylation and gene silencing is well described. Three
273 classes of HDACs exist, which have partially redundant and non-overlapping functions in the formation
274 of heterochromatin domains and gene silencing. Sir2 belongs to the class III HDAC of the sirtuin family
275 (Shankaranarayana et al. 2003). Clr3 belongs to class II and is a member of the SHREC complex
276 (Sugiyama et al. 2007). Clr6 belongs to class I and is part of several sub-complexes, contributing to both
277 heterochromatic and euchromatic gene regulation (Grewal et al. 1998; Nicolas et al. 2007). We find here
278 that unlike class III and II HDACs, sub-complexes of the Clr6 family including the Rpd3S, Rpd3L-
279 Expanded, and Clr6 I″ contribute exclusively to spreading and not nucleation (**Figure 1, 2** and **Figure**
280 **3A**, top of heatmap). In particular, we noticed that the forkhead transcription factor Fkh2, was identified
281 as a common spreading regulator in all *MAT* HSS strains. Despite not being formally annotated to the
282 Clr6 I″ complex by GO terms, Fkh2 was previously described as a member of this sub-complex (Zilio et
283 al. 2014). We included Fkh2 as a member of Clr6 I″ in further analysis for this reason. Analogous to the
284 analysis for nucleosome remodeling complexes, we represented the HDAC components that were
285 identified as hits (**Figure 3C**). The population distributions of HSS reporter fluorescence in these Clr6
286 complex mutants are shown in **Figure 3 Supplement 2**. We find an interesting bifurcation in the
287 contribution of Clr6 sub-complexes towards "loss" or "gain" categories. Clr6 I″ and Clr6S (Complex II)
288 positively contributed to spreading ("loss"), while several members of the Rpd3L-Expanded complex
289 antagonized spreading and were found as hits in the "gain" category. This includes a subset belonging to
290 the Set3 Complex (Set3, Hif2, Hos2, Snt1). Overall, this suggests that Clr6 I″ and Clr6S HDAC
291 complexes specifically promote heterochromatin spreading in addition to their described roles in
292 transcriptional gene silencing.

293 Given the strong initial phenotype of Crl6 I″ subunits in spreading (**Figure 2**), we further
294 explored their role here. Amongst the known members of Clr6 sub-complexes (**Figure 4A**), we chose

295 three subunits to validate our results: two Clr6 I″-specific members, Fkh2 and Png3, and the shared Clr6
296 core subunit Prw1. We validated the phenotypes by *de novo* single and double deletions for these genes
297 in the three *MAT* HSS reporter backgrounds (**Figure 4B-C, Figure 4 Supplement 1 A,B**) and
298 performed three-color flow cytometry to record fluorescence.

299 We first sought to validate the phenotype of these deletions in the *WT MAT* and *MAT ΔREIII*
300 HSS, which were most prominent in the screen. We found a similar phenotype for the single *Δprw1* and
301 the *Δfkh2 Δprw1* double mutant at *MAT ΔREIII,* corroborating the notion that Fkh2 is a Clr6 component
302 and acts in the same pathway as Prw1 (**Figure 4C**, bottom panels). However, we noted that the
303 phenotype of *Δprw1* was weaker than *Δfkh2* in the *WT MAT* background; nonetheless, also here the
304 double mutant showed a non-additive phenotype (**Figure 4C**, top panels). We additionally aimed to
305 validate these three deletions in the *MAT ΔcenH* HSS reporter background (**Figure 4 Supplement 1C**).
306 While this strain remains strongly repressed in the majority of the population, we detected a noticeable
307 increase in reporter signal in *Δfkh2* and *Δprw1.*

308 The above results, evidencing an impact on silencing at the spreading ("orange"), but not
309 nucleation ("green") reporter, predicted that the chromatin state may also be affected primarily at
310 nucleation-distal sites in Clr6 I″ complex mutants. We therefore next examined the chromatin state by
311 ChIP-qPCR analysis of the H3K9me2 mark at *MATΔREIII* and other heterochromatin loci. First, we
312 examined the MAT locus. Here we observed strong reductions of H3K9me2 signal at the "orange"
313 spreading reporter and also more nucleation-distal targets, in *Δfkh2, Δprw1*, and the *Δfkh2Δprw1* double
314 mutant (**Figure 4D**). There is no increase in severity of the spreading defect in the *Δfkh2Δprw1* double
315 mutant relative to the two single mutations, although further decreases in H3K9me2 should have been
316 detectable (see euchromatic target *mtd1,* **Figure 4D**). This further supports that Fkh2 and Prw1 act
317 together to promote spreading. However, consistent with the flow data, we did not observe strong

318 H3K9me2 reductions at the nucleation "green" reporter (**Figure 4D**), which is embedded in the *cenH*
319 nucleation element, except for a mild reduction in *Δfkh2*. We obtained a similar result at the related
320 pericentromeric *dh* and *dg* nucleation elements (**Figure 4 Supplement 1D**). We also find defects in
321 H3K9me2 spreading in Clr6 1″ subunit mutants at loci in addition to *MAT*. In particular, we observed
322 reduced H3K9me2 accumulation at subtelomeric targets in chromosomes I and II in *Δprw1* and *fkh2*,
323 with a stronger effect in *Δprw1* (**Figure 1E**). At the facultative heterochromatin islands *mei4, ssm4,* and
324 *mcp7*, *Δfkh2, Δprw1*, and *Δfkh2Δprw1* have similar effects as at subtelomeres (**Figure 4F**).
325 The *Δpng3* has a moderate to mild phenotype in *WT-MAT* and *MAT ΔREIII*, respectively (**Figure**
326 **4 Supplement 1A,B**). Consistent with this phenotype, we can observe a small change in H3K9me2
327 accumulation only distal to the "orange" reporter (**Figure 4D**) and a moderate effect at all
328 heterochromatin islands tested (**Figure 4F**), suggesting that Png3 plays a less prominent role than Fkh2
329 within Clr6 I″. These results evidence a defect of heterochromatin assembly in Clr6 I″ subunit mutants
330 primarily at distal, but not nucleation sites, such as *cenH* or *REIII*, indicating a surprising
331 heterochromatin-spreading specific role of Clr6 I″.
332
333 **Discussion**
334 The formation of a heterochromatin domain requires three interconnected steps, nucleation,
335 assembly of silencing structures, and the lateral spreading from DNA-sequence driven nucleation sites.
336 While the nucleation reaction has been well described, it has not been fully resolved which parts of the
337 genetic circuitry discovered to date are required for spreading. Prior studies on spreading have focused
338 primarily on factors that restrain heterochromatin formation across boundaries, which include Leo1,
339 Mst2, Epe1, Bdf2, among others (Ayoub et al. 2003; Wang et al. 2013; Verrier et al. 2015; Wang et al.
340 2015). Here, our ability to separate requirements for nucleation and distal spreading within

341 heterochromatin domains allowed us to pinpoint which factors are necessary to enable the spreading
342 reaction and factors that constrain it genome-wide. A key finding from this work is the requirement of
343 variants of the Clr6 HDAC complex specifically in the spreading reaction, in addition to the antagonism
344 by a broad class of chromatin remodelers, including Ino80, Swr1C, SWI/SNF and RSC (**Figure 3**).

345 HDACs have long been implicated in heterochromatin function generally, and here we were able
346 to distinguish which major HDACs regulate heterochromatin broadly, versus spreading specifically. The
347 Clr3 HDAC and associated SHREC complex is required for silencing, likely via its ability to repress
348 nucleosome turnover (Aygun et al. 2013), maintain nucleosome occupancy (Sugiyama et al. 2007;
349 Garcia et al. 2010), and remove H3K14 acetylation known to antagonize heterochromatin assembly
350 (Wirén et al. 2005). We find that SHREC mutants completely lose heterochromatic silencing (**Figure**
351 **1C-F, K**). Similarly, the Sir2 HDAC is broadly implicated in heterochromatin nucleation and assembly
352 (Shankaranarayana et al. 2003; Alper et al. 2013), and we also observe near-complete silencing loss in
353 *Δsir2* (**Figure 1 Supplement 2**). Clr6 complexes have been implicated in suppression of antisense
354 transcription globally, particularly complex II/Rpd3S (Nicolas et al. 2007; Yamane et al. 2011) and the
355 maintenance of heterochromatic gene silencing at major constitutive sites (Grewal et al. 1998), via the
356 recruitment by HP1/Swi6 (Fischer et al. 2009). Remarkably, we find here that particular Clr6
357 subcomplexes are specifically required for distal spreading within constitutive heterochromatin and
358 heterochromatin islands (**Figure 3,4**). Clr6 sub-complex activity is only marginally required for
359 maintaining repression at nucleation-proximal sites. This is consistent with the finding that the *clr6-1*
360 allele has only small impacts on transcription of the *cenH* nucleator-encoded ncRNAs (Yamane et al.
361 2011). We find the recently characterized Fkh2-associated complex I″ (Zilio et al. 2014) to be a central
362 player in promoting distal spread (**Figure 3,4**). This complex contains the core of complex I, Nts1,
363 Png3, Mug165 and associates with Fkh2. Not all these subunits contributed equally to regulating

364 spreading in all chromatin contexts, with Fkh2 having the strongest effect (**Figure 3, 4, Figure 3**
365 **Supplement 3** and **Figure 4 Supplement 1**). The double mutant analysis indicates that Fkh2 and Prw1
366 act together in promoting spreading (**Figure 4C**), which can be inferred from non-additive phenotype in
367 *MAT ΔREIII.* The mutants are also non-additive with respect to silencing in *WT MAT*, however *Δprw1*
368 and *Δfkh2Δprw1* phenotypes are weaker than *Δfkh2.* This type of behavior, i.e. the partial suppression of
369 phenotype by additional deletion of complex components, has been observed for silencing defects of
370 protein complexes (Barrales et al. 2016). In addition to Clr6 I″, the Alp13 and Cph1 subunits, which are
371 assigned to the separate complex II/Rpd3S (Nicolas et al. 2007) associated with global deacetylation,
372 also had positive impacts on spreading. This may indicate that (1) the composition of different Clr6
373 subcomplexes *in vivo* is either dynamic, or (2) a version of Rpd3S, jointly with a complex typified by
374 Fkh2, cooperate in promoting distal spreading of heterochromatin. Interestingly, the Set3-submodule
375 that typifies the Rpd3L-Expanded complex (Shevchenko et al. 2008), has a distinct spreading-
376 antagonizing behavior (**Figure 3C**). This contrasts with a mild positive role of the Set3 complex at
377 pericentromeres, which was proposed to be mediated indirectly, via transcriptional regulation of ClrC
378 H3K9 methylase complex genes (Yu et al. 2016).

379 We do not believe that the spreading-specific role of Clr6 complexes at the MAT locus is
380 mediated primarily by Asf/HIRA (Yamane et al. 2011), since Asf/HIRA subunits Hip1, Hip3 and Slm9
381 have mild to no phenotype for spreading in *MAT* contexts. Asf/HIRA mutant phenotypes were more
382 pronounced in *ECT*, which implies less reliance on Clr6 for spreading in *ECT* (**Figure 2**). The
383 spreading-specific role of specific Clr6 complexes may be encoded by their recruitment mechanisms.
384 HP1/Swi6, which recruits Clr6 (Fischer et al. 2009), is a known spreading regulator (Hall et al. 2002;
385 Canzio et al. 2011). Further, the Fkh2 transcription factor, which plays roles in origin coordination and
386 clustering in budding yeast (Knott et al. 2012), may play a key role in either directing Clr6 to distal sites

387 or ensuring continued association through the spreading process, which would explain its dominant roles
388 versus Png3 and other Clr6 I″ subcomplex-specific subunits (**Figure 4**, **Figure 4 Supplement 1**). The
389 precise role of Fkh2 will be the subject of further study.

390 Chromatin remodelers across several classes antagonize spreading. While Ino80 and Swr1C
391 have been linked to heterochromatin containment by specific mechanisms in budding yeast either by
392 H2A.Z exchange or preventing the invasion of euchromatin (Meneghini et al. 2003; Xue et al. 2015),
393 our results appear to indicate a more widespread effect of remodeling activities on spreading. This is
394 because in addition to Ino80 and Swr1C, the major remodeling complexes RSC and SWI/SNF also
395 contributed to spreading antagonism. A more general way remodelers have been implicated in
396 heterochromatin function is creating nucleosome free regions (NFRs, (Lorch and Kornberg 2017)) that
397 antagonize heterochromatin. Since NFRs may be roadblocks to spreading (Garcia et al. 2010;
398 Lantermann et al. 2010), it is possible that remodelers employ this mechanism to restrain
399 heterochromatin spreading globally. In addition, remodelers such as SWI/SNF and RSC destabilize
400 nucleosomes generally (Narlikar et al. 2001; Rowe and Narlikar 2010), leading to increased turnover
401 (Rawal et al. 2018), which would antagonize heterochromatin formation. This increased turnover may
402 be tolerated at ncRNA nucleation sites, where it is at near euchromatic levels (Greenstein et al. 2018),
403 likely due to ncRNA transcription (Volpe et al. 2002; Noma et al. 2004). This would indicate that
404 regulation of nucleosome stability has a particular significance at distal, but not nucleation sites.

405 Further, we found that related ncRNA nucleators in different chromatin environments require
406 distinct factors for spreading. Similarly, spreading from qualitatively different nucleators within the
407 same environment, namely *REIII* and *cenH,* also differ in their sensitivity to different mutants. The
408 significant overlap in factors between *WT MAT* and *MAT ΔREIII* indicates that heterochromatin
409 formation at MAT is dominated by the ncRNA nucleator *cenH,* in agreement with our previous findings

410 (Greenstein et al. 2018). The *REIII* element, which nucleates heterochromatin independent of ncRNA
411 (Jia et al. 2004), had different requirements. ncRNA-independent spreading is strongly antagonized by
412 the Epe1 pathway, and uniquely promoted by the MTOR pathway Gad8 kinase, partially consistent with
413 a previous report implicating Gad8 for MAT silencing (Cohen et al. 2018). The biggest difference was
414 between the MAT contexts and *ECT*. Some of the factors unique to *ECT* have been implicated in
415 inhibiting spreading across boundaries, such as Leo1 (Verrier et al. 2015), or heterochromatin stability
416 and spreading generally, such as HIRA (Yamane et al. 2011). However, these factors do not
417 significantly contribute to spreading within constitutive heterochromatin. The significant vulnerability of
418 *ECT*, compared to the similarly behaving *MAT ΔREIII* context, could be accounted by the following
419 possibilities: (1) The loss of Epe1 may impair RNAi specifically at *ECT,* nucleated by a pericentromeric
420 *dh* nucleator, but not *MAT ΔREIII,* which relies on the *dh*-homologous *cenH* nucleator (Trewick et al.
421 2007; Braun et al. 2011). (2) Alternatively, this Epe1-dependence may indicate that a naïve euchromatic
422 context is less able to compete for heterochromatin factors. *Δepe1* is known to induce heterochromatin
423 domain expansion at constitutive heterochromatin sites (Ayoub et al. 2003; Trewick et al. 2007; Braun
424 et al. 2011; Wang et al. 2015) and also heterochromatin islands (Zofall et al. 2012; Wang et al. 2015;
425 Greenstein et al. 2019), likely depleting factors available for *ECT.* This alternative would hold important
426 implications for heterochromatin formation in euchromatic contexts, which occurs throughout
427 differentiation in animal and plant systems (Ringrose and Paro 2007; Schmitz and Amasino 2007; Zylicz
428 et al. 2018). Of note, only the *ECT* context appeared to strongly require Hip1, and moderately Slm9, for
429 efficient spreading, which code for a key subunits of the HIRA H3/H4 chaperone. HIRA has been
430 implicated in stabilizing heterochromatic nucleosomes (Yamane et al. 2011) and it is possible this
431 requirement additionally highlights the challenge faced by heterochromatic domains expanding within
432 gene-rich chromatin, known to destabilize nucleosomes via transcription-associated processes.

433 In this work, we defined how regulation of heterochromatin silencing and nucleation differ in
434 fundamental ways from distal spreading. While similar nucleation elements likely rely on a common set
435 of machinery, the success of heterochromatin spreading appears much more sensitive to the chromatin
436 context, particularly if euchromatic regions are targeted for *de novo* silencing. This finding has
437 important implications for directing gene silencing of new loci appropriately, as cells change states in
438 differentiation. In these situations, regions that are previously in a transcriptionally active state are
439 invaded by heterochromatin and will have to compete for factors in a dosage limited system (Eissenberg
440 et al. 1992; Nakayama et al. 2000).

441

Acknowledgements

We thank Sy E Redding, Douglas Myers-Turnbull and Kamir Hiam for helpful discussions on data acquisition, analysis, and interpretation, and Arthur Molines for help with microscopy experiments. This work was supported by grants from the National Institutes of Health (DP2GM123484) and the UCSF Program for Breakthrough Biomedical Research (partially funded by the Sandler Foundation) to BA-S, and the ARCS Foundation Scholarship and Hooper Graduate Fellowship to RAG. HN and CT were supported by National Science Foundation Graduate Research Fellowships (grant number 1650113). This work was supported by grants awarded to SB from the European Union Network of Excellence EpiGeneSys (HEALTH-2010-257082). SB is Member of the Collaborative Research Center 1064 (Project-ID 213249687) funded by the Deutsche Forschungsgemeinschaft (DFG, German Research Foundation) and acknowledges infrastructural support. Flow cytometry and FACS data were generated in the UCSF Parnassus Flow Cytometry Core which is supported by the Diabetes Research Center (DRC) grants NIH P30 DK063720.

Materials & Methods

Strains and strain construction

Mutant Generation for Genetic Screen

For the ectopic locus HSS reporter strain, the screen was performed essentially as described (Greenstein et al. 2019). Briefly, the parent HSS reporter strain was crossed to a ~400 gene deletion mini-library (see table 1) primarily consisting of subset of the Bioneer haploid deletion and several independently validated mutants. Crosses were performed as described (Verrier et al. 2015; Barrales et al. 2016; Greenstein et al. 2019) using a RoToR HDA colony pinning robot (Singer) for ECT while for the MAT HSS reporter strains, crosses were generated using a 96 well manual pinner. In addition, for the MAT HSS strains three Δ*clr4* mutant isolates and six individual parent isolates from each genomic context were included as controls. Crosses for the MAT HSS strains were performed on ME media for 3d at 27°C, while for the ectopic HSS strain crosses were performed using SPAS media for 4d at room temperature. For all strains, crosses were incubated for 4-5d at 42°C to retain spores, while removing unmated haploid and diploid cells. For MAT HSS strains, spores were germinated on YES medium supplemented with G418 and hygromycin B. The ectopic locus HSS spores were germinated on YES medium supplemented with G418, hygromycin B, and nourseothricin. The resulting colonies were pinned into YES liquid medium for overnight growth and then prepared for flow cytometry as described below.

Validation Strain and Plasmid Construction

Plasmid constructs for gene knockout validation were generated by *in vivo* recombination as described (Greenstein et al. 2018; Greenstein et al. 2019). *S. pombe* transformants were selected as described (Greenstein et al. 2018). For microscopy, *hygMX* super-folder GFP (SFGFP) constructs for C-terminal tagging that we described previously (Al-Sady 2016) were amplified with 175bp ultramer primers with homology to *apm3* or *apl5* and transformed into a Swi6:E2C *kanMX* strain. Apm3:SFGFP;Swi6:E2C and Apl5:SFGFP;Swi6:E2C strains were selected on hygromycin B and G418. Integrations and gene knockout were confirmed by PCR.

All strains used for this study beyond the individual deletion library mutants are listed in Table 2.

Flow Cytometry

Flow cytometry data collection and normalization for genetic screen

In preparation for flow cytometry, overnight cultures were diluted to OD = 0.1 (approximately a 1:40 dilution) in rich media (YES) and incubated at 32°C with shaking of rpm for 4–6 hours. For the ectopic locus HSS strains, flow cytometry was performed essentially as described (Greenstein et al. 2018; Greenstein et al. 2019). For the MAT locus HSS strains, flow cytometry was performed using a Fortessa X20 Dual instrument (Becton Dickinson) attached with high throughput sampler (HTS) module. With a threshold of 30,000 events, samples sizes ranged from ~1000 to 30,000 cells depending on strain growth. Fluorescence detection and compensation, and data analysis were as described (Al-Sady et al. 2016; Greenstein et al. 2018; Greenstein et al. 2019). The R scripts for the screen analysis is included as a text file.

Flow cytometry data collection and normalization for validation

For validation flow cytometry experiments, cells were grown as described (Greenstein et al. 2018; Greenstein et al. 2019) with the exception that cells were diluted into YES medium and grown 5-8 hours before measurement. Flow cytometry was performed as above. Depending on strain growth and the volume collected per experiment, fluorescence values were measured for ~20,000-100,000 cells per replicate. Fluorescence detection, compensation, and data analysis were as described (Al-Sady et al. 2016; Greenstein et al. 2018; Greenstein et al. 2019)

2D-density histogram plots with ON and OFF boundary guidelines.

2D-density histogram plots (Al-Sady et al. 2016; Greenstein et al. 2018; Greenstein et al. 2019) were generated as described previously, (see (Greenstein et al. 2018) methods for Figure 4) with the following exceptions: For MAT locus strains, the guide-lines for boundary values of "off" and "on" states were determined using median of a Red-Only control plus 3 times the median absolute deviation (MAD) and median of Δ*clr4* minus 2 times the MAD value respectively. For the ECT strain, the "on" boundary guideline was calculated by median of Δ*clr4* minus one MAD value. The boundary guideline for the ECT "off" state was determined by adjusting the raw red-channel values for cells from of a no-color control strain analyzed on the same flow cytometry run to simulate a Red-Only control strain by adding the median value of the respective Δ*clr4* strain to the red value of each cell. The resulting adjusted data was used to calculate the "off" cutoff by median +3MAD as above. Validation flow cytometry plots were generated using the ggplot2 R package (Wickham 2016).

t-distributed stochastic neighbor embedding (t-SNE) analysis

Since our data varied in sample size, we transformed normalized fluorescent data into 5x5 density grids. The percentage of population residing in each of the 25 grids is represented by one variable. Increasing the number of grids to 8x8 or 10x10 did not significantly alter results. The following input settings were used before t-SNE reduction: concatenated distributions, 1000 iterations, 60 perplexity, 0 Theta. t-SNE reduction were conducted using the Rtsne package (Krijthe 2015) and the generated t-SNE model was plotted using the R packages ggplot2 (Wickham 2016).

Earth Mover's Distance (EMD) Analysis

EMD is a distance measure between two multi-dimensional distributions to evaluate the dissimilarity. EMD calculates the minimal amount of work to match the two equisized distribution (Rubner et al. 1998) The normalized fluorescent data are transformed into a 15x15 density grid as above. To calculate the fraction of change between mutant and parent population, we calculated a metric of $EMD^{mut/par}$ by taking the log2 transformation of the quotient of the EMD between mutant to *Δclr4* distributions (EMD^{mut}) by the EMD between parent to *Δclr4* distributions (EMD^{par}). For MAT HSS strains, the three *Δclr4* and six parent control isolates were respectively combined and transformed into one reference population matrix. Two-dimensional EMD between any pair of distributions in Euclidean distance are calculated using functions from the R package emdist (Urbanek and Rubner 2012).

We validated the 1000 cell cutoff for the EMD analysis by iteratively down-sampling parent strains, calculating the EMD value to the Δ*clr4* distribution, and comparing the resulting values across iterations. For each HSS parent context, all wells containing parent isolates (N=6 for MAT locus backgrounds, N=1 for ECT) were combined into one pool from which a random sample was drawn 100 times for each N = 1000, and 5000-30,000 in 5000 cell increments. For each iteration of each N number of cells, the EMD value of the down-sampled population was calculated relative to the respective Δ*clr4*

population. We calculated the mean and SD for the 100 iterations of for each N and determined that even at an N of 1000 cells in the most broadly distributed background (ECT) the SD of EMD values was <2% of the EMD value of the parent calculated from its entire distribution. Given this analysis, we conclude that while the EMD values for wells with lower cell counts will likely have higher error than those with more cells, this error is not likely to have major effects on the calculated metric.

$EMD^{mut/par}$ data were plotted in a heatmap using functions from the R package superheat (Barter and Yu 2018). Any values < -2 were converted to -2 and interpreted as such for the heatmap.

Correlation Analysis

The correlation between the $EMD^{mut/par}$ data of different pairs of genomic contexts were calculated using a linear regression model. Sir2, ClrC and SHREC are essential heterochromatin assembly factor, and their mutants have very low $EMD^{mut/par}$. These mutants were disregarded from the model fitting because they would drive the correlation. Pearson correlation coefficients and 95% confidence interval were calculated using ggscatter functions from R package ggplot2 (Wickham 2016) and ggpubr (Kassambara 2020).

Spreading Analysis

Nucleated cells were extracted using a "green"-off gate, using median of a "red"-Only control plus 2 times the SD. Enrichment of cell populations in particular "orange" fluorescence ranges ($Grid_n$) are calculated as $Grid_n^{mut/par}$: fraction of mutant population is divided by the fraction of parent population in one grid. The intervals of "orange" fluorescence used in grids are determined by: median+2SD of "orange"-OFF cells, median-1SD of "orange"-ON cells and the median of the two. To evaluate gain of spreading phenotype, enrichment in Grid 1 in *WT MAT, MAT ΔREIII and ECT* were calculated. To evaluate loss of spreading phenotype, enrichment in Grid 3 and 4 in *WT MAT* and *MAT ΔcenH,* as well as Grid 4 in *MAT ΔREIII and ECT* were calculated. The distribution of the $Grid_n^{mut/par}$ were plotted as histogram with annotation of 85th percentile and median+2SD from parent isolates. Gene hit lists comprised mutations above median and 2SD within the 85th percentile. Upset plots were generated using the R package UpSetR (Conway et al. 2017). Barplots were plotted using the R packages ggplot2 (Wickham 2016).

GO Complex and Sub-Complex analysis

<u>generating the heatmap count data</u>
GO Complexes – Based on the GO Complex annotations [link] (2019) retrieved from pombase (Lock et al. 2018), GO complex membership was determined for genes identified as hits for each strain background and hit category (gain/loss). Using functions from the R package dplyr (Wickham et al. 2020), gene names were converted to systematic ID numbers and these systematic IDs were queried against the GO complex annotation table. The number of times a GO complex appeared per background and hit category was tabulated. Genes can be associated with any number of GO complexes depending on their annotations. However, any particular gene was only counted once per GO complex despite potentially being annotated to that GO complex by more than one evidence code. The unique list of GO complexes for all hits was determined and a matrix was computed representing the number of times each

595 GO complex (row) was identified per strain/hit category (column). This counts matrix was used to
596 generate the GO complex heatmap in Figure 3A, described below.
597 Sub-complex analysis – Genes annotated to the seven complexes in Figure 3B,C were obtained from
598 pombase (Lock et al. 2018). *fkh2* was added to the Clr6 I″ complex given the protein contacts described
599 previously (Zilio et al. 2014). For the unique set of genes per panel it was determined if each gene was
600 identified as a hit in each strain background/hit category combination. The data was summarized in a
601 counts matrix where rows represent the unique list of genes per panel and columns represent the strain
602 background / hit category. The counts matrix for each set of genes was used to generate the heatmaps in
603 Figure 3B, C as described below.
604
605 <u>generating the heatmap clustering</u>
606 Using the R package ComplexHeatmap (Gu et al. 2016), both row and column dendrogram and
607 clustering were generated using hierarchical clustering. Based on an optimal Silhouette score, the strain
608 background / hit category (columns) were clustered into 3 (Figure 3A). The dendrogram representing
609 complexes (Figure 3A) in rows were not separated because validations of the clustering by connectivity,
610 Dunn index or Silhouette score were inconclusive. Clustering validations were conducted using the R
611 package clValid (Brock et al. 2008).
612
613 **Chromatin Immunoprecipitation and Quantification**
614
615 Chromatin Immunoprecipitation (ChIP) was performed essentially as described (Greenstein et al. 2018;
616 Greenstein et al. 2019) Bulk populations of cells for were grown overnight to saturation in YES
617 medium. The following morning, cultures were diluted to OD 0.1 in 25mL YES and grown for 8h at
618 32°C and 225rpm. Based on OD measurements, $60x10^6$ cells were fixed and processed for ChIP as
619 previously described (Greenstein et al. 2018) without the addition of W303 carrier. Cleared chromatin
620 for each ChIP sample was incubated with 1µL of anti-H3K9me2 antibody (Abcam, ab1220) overnight
621 after a small fraction was retained as Input/WCE. DNAs were quantified by RT-qPCR and percent
622 immunoprecipitation (%IP, ChIP DNA/Input DNA*100) was calculated as described (Greenstein et al.
623 2018). Data for %IP was plotted using the R packages ggplot2 (Wickham 2016) and dplyr (Wickham et
624 al. 2020).
625
626 **Microscopy**
627
628 Swi6:E2C; Apl5:SFGFP and Swi6:E2C; Apm3:SFGFP cells were grown is YS media as described.
629 Slides (ibidi, Cat. No. 80606) were pre-coated with 100 mg/mL lectin (Sigma-Aldrich, Cat. No. L1395)
630 diluted in water by adding lectin solution to slide for 1 min. and removing supernatant. Log-phase
631 growing cells were applied to the slide and excess cells were rinsed off with YS. Cells were immediately
632 imaged with a 60x objective (CFI Plan Apochromat VC 60XC WI) on a Nikon TI-E equipped with a
633 spinning-disk confocal head (CSU10, Yokogawa) and an EM-CCD camera (Hammamatsu). Cells were
634 imaged in brightfield and additionally excited with 488nm (SFGFP) and 561nm (E2C) lasers. Emission
635 was collected using a 510/50 band-pass filter for GFP emission and a 600/50 band-pass filter for E2C
636 emission. For the SFGFP and E2C channels, z-stacks were obtained at 0.3µm/slice for 11 slices total.
637 An overlay of the maximum z-projections for SFGFP and E2C channels are shown separately from the
638 brightfield images. Brightness and contrast were adjusted in ImageJ to clearly show both Swi6 and
639 Apl5/Apm5 signals in the overlay. At least 2 isolates were imaged to confirm localization patterns.
640

Data Availability

Screen flow cytometry data and analysis scripts will be made available upon publication of the manuscript.

646 **References**

647 Al-Sady B, Greenstein RA, El-Samad HJ, Braun S, Madhani HD. 2016. Sensitive and Quantitative Three-Color
648 Protein Imaging in Fission Yeast Using Spectrally Diverse, Recoded Fluorescent Proteins with
649 Experimentally-Characterized In Vivo Maturation Kinetics. *PloS one* **11**: e0159292.
650 Al-Sady B, Madhani HD, Narlikar GJ. 2013. Division of labor between the chromodomains of HP1 and Suv39
651 methylase enables coordination of heterochromatin spread. *Mol Cell* **51**: 80-91.
652 Alabert C, Barth TK, Reveron-Gomez N, Sidoli S, Schmidt A, Jensen ON, Imhof A, Groth A. 2015. Two distinct
653 modes for propagation of histone PTMs across the cell cycle. *Genes & development* **29**: 585-590.
654 Alper BJ, Job G, Yadav RK, Shanker S, Lowe BR, Partridge JF. 2013. Sir2 is required for Clr4 to initiate
655 centromeric heterochromatin assembly in fission yeast. *The EMBO journal* **32**: 2321-2335.
656 Aygun O, Mehta S, Grewal SI. 2013. HDAC-mediated suppression of histone turnover promotes epigenetic
657 stability of heterochromatin. *Nature structural & molecular biology* **20**: 547-554.
658 Ayoub N, Goldshmidt I, Lyakhovetsky R, Cohen A. 2000. A fission yeast repression element cooperates with
659 centromere-like sequences and defines a mat silent domain boundary. *Genetics* **156**: 983-994.
660 Ayoub N, Noma K-i, Isaac S, Kahan T, Grewal SIS, Cohen A. 2003. A novel jmjC domain protein modulates
661 heterochromatization in fission yeast. *Molecular and cellular biology* **23**: 4356-4370.
662 Barrales RR, Forn M, Georgescu PR, Sarkadi Z, Braun S. 2016. Control of heterochromatin localization and
663 silencing by the nuclear membrane protein Lem2. *Genes & development* **30**: 133-148.
664 Barter RL, Yu B. 2018. Superheat: An R package for creating beautiful and extendable heatmaps for visualizing
665 complex data. *Journal of computational and graphical statistics : a joint publication of American*
666 *Statistical Association, Institute of Mathematical Statistics, Interface Foundation of North America* **27**:
667 910-922.
668 Bayne EH, Bijos DA, White SA, de Lima Alves F, Rappsilber J, Allshire RC. 2014. A systematic genetic screen
669 identifies new factors influencing centromeric heterochromatin integrity in fission yeast. *Genome biology*
670 **15**: 481.
671 Braun S, Garcia JF, Rowley M, Rougemaille M, Shankar S, Madhani HD. 2011. The Cul4-Ddb1(Cdt)(2)
672 ubiquitin ligase inhibits invasion of a boundary-associated antisilencing factor into heterochromatin. *Cell*
673 **144**: 41-54.
674 Brock G, Pihur V, Datta S, Datta S. 2008. clValid: An R Package for Cluster Validation *Journal of Statiscal*
675 *Software* **25**: http://www.jstatsoft.org/v25/i04.
676 Buhler M, Haas W, Gygi SP, Moazed D. 2007. RNAi-dependent and -independent RNA turnover mechanisms
677 contribute to heterochromatic gene silencing. *Cell* **129**: 707-721.
678 Canzio D, Chang EY, Shankar S, Kuchenbecker KM, Simon MD, Madhani HD, Narlikar GJ, Al-Sady B. 2011.
679 Chromodomain-mediated oligomerization of HP1 suggests a nucleosome-bridging mechanism for
680 heterochromatin assembly. *Mol Cell* **41**: 67-81.
681 Canzio D, Liao M, Naber N, Pate E, Larson A, Wu S, Marina DB, Garcia JF, Madhani HD, Cooke R et al. 2013.
682 A conformational switch in HP1 releases auto-inhibition to drive heterochromatin assembly. *Nature* **496**:
683 377-381.
684 Cohen A, Habib A, Laor D, Yadav S, Kupiec M, Weisman R. 2018. TOR complex 2 in fission yeast is required
685 for chromatin-mediated gene silencing and assembly of heterochromatic domains at subtelomeres. *The*
686 *Journal of biological chemistry* **293**: 8138-8150.
687 Consortium TGO. 2019. The Gene Ontology Resource: 20 years and still GOing strong. *Nucleic acids research*
688 **47**: D330-d338.
689 Conway JR, Lex A, Gehlenborg N. 2017. UpSetR: an R package for the visualization of intersecting sets and their
690 properties. *Bioinformatics (Oxford, England)* **33**: 2938-2940.
691 Eissenberg JC, Morris GD, Reuter G, Hartnett T. 1992. The heterochromatin-associated protein HP-1 is an
692 essential protein in Drosophila with dosage-dependent effects on position-effect variegation. *Genetics*
693 **131**: 345-352.

694 Fischer T, Cui B, Dhakshnamoorthy J, Zhou M, Rubin C, Zofall M, Veenstra TD, Grewal SIS. 2009. Diverse
695 roles of HP1 proteins in heterochromatin assembly and functions in fission yeast. *Proc Natl Acad Sci USA*
696 **106**: 8998-9003.
697 Garcia JF, Dumesic PA, Hartley PD, El-Samad H, Madhani HD. 2010. Combinatorial, site-specific requirement
698 for heterochromatic silencing factors in the elimination of nucleosome-free regions. *Genes &*
699 *development* **24**: 1758-1771.
700 Greenstein RA, Barrales RR, Sanchez NA, Bisanz JE, Braun S, Al-Sady B. 2019. Set1/COMPASS repels
701 heterochromatin invasion at euchromatic sites by disrupting Suv39/Clr4 activity and nucleosome stability.
702 *Genes & development* **34**: 99-117.
703 Greenstein RA, Jones SK, Spivey EC, Rybarski JR, Finkelstein IJ, Al-Sady B. 2018. Noncoding RNA-nucleated
704 heterochromatin spreading is intrinsically labile and requires accessory elements for epigenetic stability.
705 *eLife* **7**.
706 Grewal SIS, Bonaduce MJ, Klar AJS. 1998. Histone deacetylase homologs regulate epigenetic inheritance of
707 transcriptional silencing and chromosome segregation in fission yeast. *Genetics* **150**: 563-576.
708 Grewal SIS, Klar AJS. 1996. Chromosomal inheritance of epigenetic states in fission yeast during mitosis and
709 meiosis. *Cell* **86**: 95-101.
710 Gu Z, Eils R, Schlesner M. 2016. HilbertCurve: an R/Bioconductor package for high-resolution visualization of
711 genomic data. *Bioinformatics (Oxford, England)* **32**: 2372-2374.
712 Hall IM, Shankaranarayana GD, Noma KI, Ayoub N, Cohen A, Grewal SIS. 2002. Establishment and
713 maintenance of a heterochromatin domain. *Science* **297**: 2232-2237.
714 Hansen KR, Hazan I, Shanker S, Watt S, Verhein-Hansen J, Bahler J, Martienssen RA, Partridge JF, Cohen A,
715 Thon G. 2011. H3K9me-independent gene silencing in fission yeast heterochromatin by Clr5 and histone
716 deacetylases. *PLoS genetics* **7**: e1001268.
717 Hansen KR, Ibarra PT, Thon G. 2006. Evolutionary-conserved telomere-linked helicase genes of fission yeast are
718 repressed by silencing factors, RNAi components and the telomere-binding protein Taz1. *Nucleic acids*
719 *research* **34**: 78-88.
720 Jacobs SA, Taverna SD, Zhang YN, Briggs SD, Li JM, Eissenberg JC, Allis CD, Khorasanizadeh S. 2001.
721 Specificity of the HP1 chromo domain for the methylated N-terminus of histone H3. *Embo Journal* **20**:
722 5232-5241.
723 Jia S, Noma K, Grewal SI. 2004. RNAi-independent heterochromatin nucleation by the stress-activated
724 ATF/CREB family proteins. *Science* **304**: 1971-1976.
725 Kassambara A. 2020. ggpubr: 'ggplot2' Based Publication Ready Plots. https://CRAN.R-
726 project.org/package=ggpubr.
727 Keller C, Woolcock K, Hess D, Bühler M. 2010. Proteomic and functional analysis of the noncanonical poly(A)
728 polymerase Cid14. *RNA (New York, NY)* **16**: 1124-1129.
729 Kim HS, Choi ES, Shin JA, Jang YK, Park SD. 2004. Regulation of Swi6/HP1-dependent heterochromatin
730 assembly by cooperation of components of the mitogen-activated protein kinase pathway and a histone
731 deacetylase Clr6. *The Journal of biological chemistry* **279**: 42850-42859.
732 Knott SR, Peace JM, Ostrow AZ, Gan Y, Rex AE, Viggiani CJ, Tavaré S, Aparicio OM. 2012. Forkhead
733 transcription factors establish origin timing and long-range clustering in S. cerevisiae. *Cell* **148**: 99-111.
734 Krijthe JH. 2015. Rtsne: T-Distributed Stochastic Neighbor Embedding using a Barnes-Hut Implementation.
735 https://github.com/jkrijthe/Rtsne.
736 Lachner M, O'Carroll N, Rea S, Mechtler K, Jenuwein T. 2001. Methylation of histone H3 lysine 9 creates a
737 binding site for HP1 proteins. *Nature* **410**: 116-120.
738 Lantermann AB, Straub T, Stralfors A, Yuan GC, Ekwall K, Korber P. 2010. Schizosaccharomyces pombe
739 genome-wide nucleosome mapping reveals positioning mechanisms distinct from those of Saccharomyces
740 cerevisiae. *Nature structural & molecular biology* **17**: 251-U215.
741 Lee J, Choi ES, Seo HD, Kang K, Gilmore JM, Florens L, Washburn MP, Choe J, Workman JL, Lee D. 2017.
742 Chromatin remodeller Fun30(Fft3) induces nucleosome disassembly to facilitate RNA polymerase II
743 elongation. *Nature communications* **8**: 14527.

744 Lejeune E, Bortfeld M, White SA, Pidoux AL, Ekwall K, Allshire RC, Ladurner AG. 2007. The chromatin-
745 remodeling factor FACT contributes to centromeric heterochromatin independently of RNAi. *Current*
746 *biology : CB* **17**: 1219-1224.
747 Lock A, Rutherford K, Harris MA, Hayles J, Oliver SG, Bähler J, Wood V. 2018. PomBase 2018: user-driven
748 reimplementation of the fission yeast database provides rapid and intuitive access to diverse,
749 interconnected information. *Nucleic acids research* **47**: D821-D827.
750 Lorch Y, Kornberg RD. 2017. Chromatin-remodeling for transcription. *Quarterly reviews of biophysics* **50**: e5.
751 Marina DB, Shankar S, Natarajan P, Finn KJ, Madhani HD. 2013. A conserved ncRNA-binding protein recruits
752 silencing factors to heterochromatin through an RNAi-independent mechanism. *Genes & development* **27**:
753 1851-1856.
754 Meneghini MD, Wu M, Madhani HD. 2003. Conserved histone variant H2A.Z protects euchromatin from the
755 ectopic spread of silent heterochromatin. *Cell* **112**: 725-736.
756 Moazed D. 2009. Small RNAs in transcriptional gene silencing and genome defence. *Nature* **457**: 413-420.
757 Nakayama J, Klar AJ, Grewal SI. 2000. A chromodomain protein, Swi6, performs imprinting functions in fission
758 yeast during mitosis and meiosis. *Cell* **101**: 307-317.
759 Narlikar GJ, Phelan ML, Kingston RE. 2001. Generation and Interconversion of Multiple Distinct Nucleosomal
760 States as a Mechanism for Catalyzing Chromatin Fluidity. *Mol Cell* **8**: 1219-1230.
761 Nicetto D, Zaret KS. 2019. Role of H3K9me3 heterochromatin in cell identity establishment and maintenance.
762 *Current opinion in genetics & development* **55**: 1-10.
763 Nicolas E, Yamada T, Cam HP, FitzGerald PC, Kobayashi R, Grewal SIS. 2007. Distinct roles of HDAC
764 complexes in promoter silencing, antisense suppression and DNA damage protection. *Nature structural &*
765 *molecular biology* **14**: 372-380.
766 Noma K, Sugiyama T, Cam H, Verdel A, Zofall M, Jia S, Moazed D, Grewal SI. 2004. RITS acts in cis to
767 promote RNA interference-mediated transcriptional and post-transcriptional silencing. *Nature genetics*
768 **36**: 1174-1180.
769 Orlova DY, Zimmerman N, Meehan S, Meehan C, Waters J, Ghosn EE, Filatenkov A, Kolyagin GA, Gernez Y,
770 Tsuda S et al. 2016. Earth Mover's Distance (EMD): A True Metric for Comparing Biomarker Expression
771 Levels in Cell Populations. *PloS one* **11**: e0151859.
772 Ragunathan K, Jih G, Moazed D. 2015. Epigenetics. Epigenetic inheritance uncoupled from sequence-specific
773 recruitment. *Science* **348**: 1258699.
774 Rawal Y, Chereji RV, Qiu H, Ananthakrishnan S, Govind CK, Clark DJ, Hinnebusch AG. 2018. SWI/SNF and
775 RSC cooperate to reposition and evict promoter nucleosomes at highly expressed genes in yeast. *Genes &*
776 *development* **32**: 695-710.
777 Reyes-Turcu FE, Zhang K, Zofall M, Chen E, Grewal SI. 2011. Defects in RNA quality control factors reveal
778 RNAi-independent nucleation of heterochromatin. *Nat Struct Mol Biol* **18**: 1132-1138.
779 Ringrose L, Paro R. 2007. Polycomb/Trithorax response elements and epigenetic memory of cell identity.
780 *Development* **134**: 223-232.
781 Rowe CE, Narlikar GJ. 2010. The ATP-dependent remodeler RSC transfers histone dimers and octamers through
782 the rapid formation of an unstable encounter intermediate. *Biochemistry* **49**: 9882-9890.
783 Rubner Y, Tomasi C, Guibas LJ. 1998. A metric for distributions with applications to image databases. . in *IEEE*
784 *International Conference on Computer Vision*, pp. 59-66.
785 Schmitz RJ, Amasino RM. 2007. Vernalization: a model for investigating epigenetics and eukaryotic gene
786 regulation in plants. *Biochimica et biophysica acta* **1769**: 269-275.
787 Scott KC, Merrett SL, Willard HF. 2006. A heterochromatin barrier partitions the fission yeast centromere into
788 discrete chromatin domains. *Current biology : CB* **16**: 119-129.
789 Shankaranarayana GD, Motamedi MR, Moazed D, Grewal SIS. 2003. Sir2 regulates histone H3 lysine 9
790 methylation and heterochromatin assembly in fission yeast. *Current Biology* **13**: 1240-1246.
791 Shevchenko A, Roguev A, Schaft D, Buchanan L, Habermann B, Sakalar C, Thomas H, Krogan NJ, Shevchenko
792 A, Stewart AF. 2008. Chromatin Central: towards the comparative proteome by accurate mapping of the
793 yeast proteomic environment. *Genome biology* **9**: R167.

794 Sugiyama T, Cam HP, Sugiyama R, Noma K-i, Zofall M, Kobayashi R, Grewal SIS. 2007. SHREC, an effector
795 complex for heterochromatic transcriptional silencing. *Cell* **128**: 491-504.
796 Thon G, Bjerling KP, Nielsen IS. 1999. Localization and properties of a silencing element near the mat3-M
797 mating-type cassette of Schizosaccharomyces pombe. *Genetics* **151**: 945-963.
798 Trewick SC, Minc E, Antonelli R, Urano T, Allshire RC. 2007. The JmjC domain protein Epe1 prevents
799 unregulated assembly and disassembly of heterochromatin. *The EMBO journal* **26**: 4670-4682.
800 Urbanek S, Rubner Y. 2012. emdist: earth mover's distance. https://CRAN.R-project.org/package=emdist.
801 Verrier L, Taglini F, Barrales RR, Webb S, Urano T, Braun S, Bayne EH. 2015. Global regulation of
802 heterochromatin spreading by Leo1. *Open biology* **5**.
803 Volpe TA, Kidner C, Hall IM, Teng G, Grewal SIS, Martienssen RA. 2002. Regulation of heterochromatic
804 silencing and histone H3 lysine-9 methylation by RNAi. *Science* **297**: 1833-1837.
805 Wang J, Cohen AL, Letian A, Tadeo X, Moresco JJ, Liu J, Yates JR, 3rd, Qiao F, Jia S. 2016. The proper
806 connection between shelterin components is required for telomeric heterochromatin assembly. *Genes &*
807 *development* **30**: 827-839.
808 Wang J, Reddy BD, Jia S. 2015. Rapid epigenetic adaptation to uncontrolled heterochromatin spreading. *eLife* **4**.
809 Wang J, Tadeo X, Hou H, Tu PG, Thompson J, Yates JR, 3rd, Jia S. 2013. Epe1 recruits BET family
810 bromodomain protein Bdf2 to establish heterochromatin boundaries. *Genes & development* **27**: 1886-
811 1902.
812 Wen B, Wu H, Shinkai Y, Irizarry RA, Feinberg AP. 2009. Large histone H3 lysine 9 dimethylated chromatin
813 blocks distinguish differentiated from embryonic stem cells. *Nature genetics* **41**: 246-250.
814 Wickham H. 2016. *ggplot2: Elegant Graphics for Data Analysis*. Springer
815 Wickham H, François R, Henry L, Müller K. 2020. dplyr: A Grammar of Data Manipulation. in *R package*
816 *version 0 8 4* https://CRAN.R-project.org/package=dplyr.
817 Wirén M, Silverstein RA, Sinha I, Walfridsson J, Lee H-M, Laurenson P, Pillus L, Robyr D, Grunstein M, Ekwall
818 K. 2005. Genomewide analysis of nucleosome density histone acetylation and HDAC function in fission
819 yeast. *The EMBO journal* **24**: 2906-2918.
820 Xue Y, Van C, Pradhan SK, Su T, Gehrke J, Kuryan BG, Kitada T, Vashisht A, Tran N, Wohlschlegel J et al.
821 2015. The Ino80 complex prevents invasion of euchromatin into silent chromatin. *Genes & development*
822 **29**: 350-355.
823 Yamane K, Mizuguchi T, Cui B, Zofall M, Noma K, Grewal SI. 2011. Asf1/HIRA facilitate global histone
824 deacetylation and associate with HP1 to promote nucleosome occupancy at heterochromatic loci. *Mol*
825 *Cell* **41**: 56-66.
826 Yu Y, Zhou H, Deng X, Wang W, Lu H. 2016. Set3 contributes to heterochromatin integrity by promoting
827 transcription of subunits of Clr4-Rik1-Cul4 histone methyltransferase complex in fission yeast. *Sci Rep* **6**:
828 31752.
829 Zhang K, Mosch K, Fischle W, Grewal SIS. 2008. Roles of the Clr4 methyltransferase complex in nucleation,
830 spreading and maintenance of heterochromatin. *Nature structural & molecular biology* **15**: 381-388.
831 Zhu J, Adli M, Zou JY, Verstappen G, Coyne M, Zhang X, Durham T, Miri M, Deshpande V, De Jager PL et al.
832 2013. Genome-wide chromatin state transitions associated with developmental and environmental cues.
833 *Cell* **152**: 642-654.
834 Zilio N, Codlin S, Vashisht AA, Bitton DA, Head SR, Wohlschlegel JA, Bähler J, Boddy MN. 2014. A novel
835 histone deacetylase complex in the control of transcription and genome stability. *Molecular and cellular*
836 *biology* **34**: 3500-3514.
837 Zofall M, Smith DR, Mizuguchi T, Dhakshnamoorthy J, Grewal SIS. 2016. Taz1-Shelterin Promotes Facultative
838 Heterochromatin Assembly at Chromosome-Internal Sites Containing Late Replication Origins. *Mol Cell*
839 **62**: 862-874.
840 Zofall M, Yamanaka S, Reyes-Turcu FE, Zhang K, Rubin C, Grewal SI. 2012. RNA elimination machinery
841 targeting meiotic mRNAs promotes facultative heterochromatin formation. *Science* **335**: 96-100.
842 Zylicz JJ, Borensztein M, Wong FC, Huang Y, Lee C, Dietmann S, Surani MA. 2018. G9a regulates temporal
843 preimplantation developmental program and lineage segregation in blastocyst. *eLife* **7**.

844 Zylicz JJ, Dietmann S, Gunesdogan U, Hackett JA, Cougot D, Lee C, Surani MA. 2015. Chromatin dynamics and
845 the role of G9a in gene regulation and enhancer silencing during early mouse development. *eLife* **4**.

846

847 **FIGURE LEGENDS**
848
849 **Figure 1: A genetic screen based on a suite of fluorescent reporters identifies context-**
850 **dependent positive and negative regulators of heterochromatin function.**
851
852 **A.** TOP: Overview of heterochromatin spreading sensor (HSS, Greenstein 2018). Three
853 transcriptionally encoded fluorescent protein genes are integrated in the genome. *SFGFP* ("green")
854 proximal to the nucleation site allows identification of heterochromatin nucleation; *mKO2* ("orange")
855 distal to the nucleation site allows identification of heterochromatin spreading. *3xE2C* ("red") in a
856 euchromatin region normalizes cell-to-cell noise. BOTTOM: The endogenous mating type locus (*MAT*)
857 and ectopically heterochromatic *ura4* locus (Greenstein 2018) were examined with the HSS in the
858 screen. *Bona fide* mutations of the nucleators, *cenH* and *REIII*, in *MAT* were made to limit nucleation to
859 occur from one site.

860 **B.** Overview of data processing for t-SNE. The multidimensional fluorescence data is linearized before
861 subjection to t-SNE. Two-dimensional "orange"/"red" *v.* "green"/"red" density plots are broken down into
862 25 grids in an unbiased manner, and normalized cell counts of each grid are used as parameters for
863 each mutant in the t-SNE processing. The 25 parameters of all mutants from all chromatin contexts
864 were embedded into a model two-dimensional t-SNE space.
865
866 **C.-F.** 2D-density hexbin plots of the wild-type parent or *Δclr3* mutant in the (**C**) *WT MAT,* (**D**) *MAT*
867 *ΔcenH,* (**E**)*MAT ΔREIII,* and (**F**) *ECT* background. Hexagonal bins are colored from light grey to black
868 indicating low to high density of cells per bin. Blue lines indicate boundary guidelines for the fully
869 repressed state and red lines indicate boundary guidelines values for fully expressed state (see
870 methods for treatment of MAT and ECT strains)

871 **G-I.** t-SNE visualization of all mutants across all four chromatin contexts. Each data point represents a
872 mutant, the fill color represents the (**G**) chromatin context of the mutant, or median (**H**) "green" or (**I**)
873 "orange" fluorescence of the entire mutant population. In (**H**) the parent isolates of each background are
874 depicted in individual colors indicated in the key. In (**I**), selected mutants are shown, with the chromatin
875 contexts highlighted with the same colors as (C-F). An enlarged region to highlight the *Δclr3* mutants is
876 shown to the right.

877
878 **J.** To linearize the multidimensional fluorescence data, the earth mover's distance (EMD) between each
879 mutant and a *Δclr4* mutant is calculated. $EMD^{mut/par}$ is computed by dividing each mutant EMD (EMD^{mut})
880 by the respective parent EMD (EMD^{par}) and transforming the quotient by log2.
881
882 **K.** Heatmaps depicting $EMD^{mut/par}$ of indicated mutants in each chromatin context. Any values <-2 were
883 converted to -2 and interpreted as such. Crossed-out boxes indicate mutants excluded from the
884 analysis due to growth defect or low sample size.
885
886 **Figure 2: Identification of heterochromatin spreading regulators in different chromatin contexts.**
887
888 **A.** Overview of the spreading-specific analysis with mock distributions of cells and grids indicated. To
889 segregate spreading from nucleation or silencing phenotypes, "green"-off populations (successful
890 nucleation events) are isolated. Within these populations, enrichment of cell populations in particular
891 "orange" fluorescence ranges ($Grid_n$) are calculated as $Grid_n^{mut/par}$. *E.g.* to identify loss of spreading
892 mutants in *WT MAT*, $Grid_{3+4}^{mut/par}$ is calculated as percentage of mutant population divided by
893 percentage of parent population in $Grid_{3+4}$ (green, blue). The Grids used for analysis of gain and loss of

894 spreading in the four chromatin contexts are indicated. $Grid_{3+4}$ was used for *WT MAT* and *MAT ΔcenH,*
895 given the highly repressed nature of this chromatin context.
896
897 **B.-C.** Upset plots indicating the frequency of (**B**) Loss of Spreading, or (**C**) Gain of Spreading gene hits
898 appearing in one or multiple chromatin contexts. For each bar, the chromatin context(s) with shared
899 phenotypes for the underlying gene hits is indicated below the plot. The inset indicates the total number
900 gene hits in each chromatin context of the same phenotype.
901
902 **D.-G.** Bar graphs representing the $Grid_n^{mut/par}$ and number of chromatin context(s) of gene hits with Loss
903 of Spreading phenotype from (**D**) *WT MAT*, (**E**) *MAT ΔcenH,* (**F**) *MAT ΔREIII* and (**G**) *ECT* respectively.
904 The genes are ranked in descending order of $Grid_n^{mut/par}$ and the color of each bar represents the
905 number of backgrounds the mutant show the same phenotype.
906
907 **H.-I.** 2D-density hexbin plots of the top two loss of spreading gene hits for all 4 chromatin contexts, (**H**)
908 *WT MAT,* (**I**) *MAT ΔcenH,* (**J**) *MAT ΔREIII,* and (**K**) *ECT*. Plotting as in Figure 1, C-F. For wild-type
909 comparison, see Figure 1 C-F.
910
911
912 **Figure 3: Heterochromatin spreading is regulated by sets of unique and common protein**
913 **complexes across different chromatin contexts.**
914
915 **A.** Heatmap of GO complex annotations for hits in each category and strain. Rows, representing GO
916 complexes annotated to genes within the screen that were identified as hits, are arranged via
917 hierarchical clustering. Columns are defined by the hit category (loss of spreading – white; gain of
918 spreading – black), and each screen chromatin context is indicated at the top. The columns were
919 clustered by hierarchical clustering and the tree was cut to define 3 clusters.
920
921 **B.** Hit table of complex members for Swr1C, Ino80, SWI/SNF, and RSC-type complexes. Components
922 identified as a hit in either the "gain" or "loss" category for each background are marked blue. Columns
923 are defined and ordered as in (**A**). The proteins present in each complex are annotated at the right with
924 the presence of color indicating membership of that protein in the complex.
925
926 **C.** Hit table of complex members for Rpd3L-Expanded, Rpd3S, and Clr6 complex I" as in (**B**). Columns
927 are defined and ordered as in (**A**) Proteins present in each complex are annotated as in (**B**).
928
929 **Figure 4: Clr6 Complex I" regulates heterochromatin spreading at constitutive and facultative**
930 **heterochromatin loci.**
931
932 **A.** Cartoon of Clr6 complexes (Clr6L, the Clr6LExpanded modules, Clr6 subcomplex 1", and Clr6S).
933 Subunits not in the screen are shown in grey.
934
935 **B.** Scheme for generation of deletion mutants. Double mutant of fkh2 and prw1 was generated by both
936 cross and *de novo* deletion of *prw1* in *Δfkh2*.
937
938 **C.** TOP PANELS: 2D-density hexbin plots for WT and Clr6 I" mutants in the *WT MAT* strain
939 background. Hexagonal bins are colored from light grey to black indicating low to high density of cells
940 per bin. A rug plot is included on the X and Y axes indicating the 1D density for each color. Rug lines
941 are colored with partial transparency to assist with visualization of density changes. Blue lines indicate
942 boundary guidelines for the fully repressed state and red lines indicate boundary guidelines values for
943 fully expressed state as in Figure 1.

944 BOTTOM PANELS: 2D-density hexbin plots with rug as above for WT and Clr6 I" mutants in the *MAT*
945 *ΔREIII* strain background.
946
947 **D.-F.** ChIP-qPCR quantification of H3K9me2 signal in the *MAT ΔREIII* strain at constitutive and
948 facultative heterochromatin regions. Error bars represent 1SD from three biological replicate isolates.
949 Individual values are plotted for each isolate. The WT data is additionally replicated in Figure 3
950 Supplement 2 as these experiments were performed together. SD; standard deviation. Telomere 1L
951 primer distances are from the end of the assembled genomic sequence.
952
953 **Figure 1 Supplement 1: Screen overview.**
954
955 **A.** Schematic of the screen to identify genes that contribute to heterochromatin nucleation and
956 spreading. A custom nuclear function deletion library (Table 1) was mated with four different reporter
957 strains (*WT MAT, MAT ΔcenH, MAT ΔREIII and ECT*). The fluorescences of "green", "orange" and
958 "red" for each mutant cell within each background are recorded by flow cytometry.
959
960 **Figure 1 Supplement 2: Pairwise plots depicting the comparisons of mutant $EMD^{mut/par}$.**
961
962 Pairwise plots depicting the $EMD^{mut/par}$ comparisons of (**A**) *MAT ΔcenH* with *WT MAT,* (**B**) *MAT ΔREIII*
963 with *WT MAT,* (**C**) *ECT* with *WT MAT,* (**D**) *MAT ΔREIII* with *MAT ΔcenH,* (**E**) *ECT* with *MAT ΔcenH* and
964 (**F**) *ECT* with *MAT ΔREIII*. Pearson correlation coefficients (ρ), determined without SHREC, ClrC
965 mutants and *Δsir2*, were calculated and correlations plotted for A, B and D.
966
967 **Figure 2 Supplement 1: The distribution of $Grid_n^{mut/par}$ of all mutants in the loss or gain of**
968 **spreading hit categories.**
969
970 **A.-D.** Histograms representing the distribution of $Grid_n^{mut/par}$ of (**A**) *WT MAT*, (**B**) *MAT ΔcenH,* (**C**) *MAT*
971 *ΔREIII* and (**D**) *ECT* in the loss of spreading hit category. The red line indicates two standard deviation
972 above median of parent isolates. The dashed blue line indicates the 85th percentile.
973
974 **E.-G.** Histograms representing the distribution of $Grid_n^{mut/par}$ of (**E**) *WT MAT,* (**F**) *MAT ΔREIII* and (**G**)
975 *ECT* in the gain of spreading hit category. The red line indicates two standard deviation above median
976 of parent isolates. The dashed blue line indicates the 85th percentile.
977
978 **Figure 2 Supplement 2: $Grid_n^{mut/par}$ and overlapped chromatin contexts of identified gain of**
979 **spreading mutants**
980
981 **A.-C.** Bar graphs representing the $Grid_n^{mut/par}$ and number of overlapped chromatin context(s) of gene
982 hits with Gain of Spreading phenotype in (**A**) *WT MAT*, (**B**) *MAT ΔREIII* and (**C**) *ECT* chromatin
983 contexts respectively. The genes are ranked in descending order of $Grid_n^{mut/par}$ and the color of each bar
984 represents the number of backgrounds the mutant show the same phenotype.
985
986 **D.-F.** 2D-density hexbin plots of the top two gain of spreading gene hits for all 3 chromatin contexts, (**D**)
987 *WT MAT,* (**E**) *MAT ΔREIII,* and (**F**) *ECT*. Plotting as in Figure 1, C-F. For wild-type comparison, see
988 Figure 1 C-F.
989
990 **Figure 3 Supplement 1: Original 2D density histograms for chromatin remodeler gain of**
991 **spreading hits.**
992

993 **A.** Chromatin remodeler gain of spreading gene hits for *MAT ΔREIII.* Original 2D density histograms for
994 all the gain of spreading gene hits from Figure 3B are shown. **B.** Chromatin remodeler gain of
995 spreading gene hits for *ECT.* Original 2D density histograms for all the gain of spreading gene hits from
996 Figure 3B are shown. GO complex annotations are indicated next to each mutant. 2D density
997 histograms as in Figure 1 C-F. Original *MAT ΔREIII* and *ECT* parents shown in Figure 1 are reproduced
998 here again (with transparency) for comparison. Mutants within each chromatin next are shown in
999 descending order of their $Grid_n^{mut/par}$ values.
1000
1001 **Figure 3 Supplement 2: *Δapm3* has a mild heterochromatin spreading phenotype and the**
1002 **protein is distributed in the cytosol and nucleus.**
1003

1004 **A.-D.** ChIP-qPCR quantification of H3K9me2 signal in the *MAT ΔREIII* strain at constitutive and
1005 facultative heterochromatin regions in wild-type and an independently generated *Δapm3* alleles. Error
1006 bars represent 1SD from three biological replicate isolates. Individual values are plotted for each
1007 isolate. The WT data is additionally replicated in Figure 4 as these experiments were performed
1008 together.

1009 **E.** Apm3:SFGFP is distributed in the cytosol and nucleus. Apm3:SFGFP was expressed from its native
1010 locus and co-expressed with Swi6:E2C. Swi6:E2C labels nuclear heterochromatin. Z-projection
1011 overlays of the Apm3:SFGFP and Swi6:E2C on top, and a brightfield image on the bottom.

1012 **F.** Apl5:SFGFP is largely nuclear excluded. Apl5:SFGFP was expressed from its native locus and co-
1013 expressed with Swi6:E2C. Swi6:E2C labels nuclear heterochromatin. Z-projection overlays of the
1014 Apl5:SFGFP and Swi6:E2C on top, and a brightfield image on the bottom.

1015
1016
1017 **Figure 3 Supplement 3: Original 2D density histogram for all Clr6 complex subunit mutants in**
1018 ***MAT ΔREIII.***
1019
1020 Original 2D density histograms of all Clr6 complexes gene mutants corresponding to Figure 3C in *MAT*
1021 *ΔREIII* context. Original *MAT ΔREIII* wild type parent and *Δfkh2* and *Δprw1* mutants shown in Figures 1
1022 and 4 are reproduced here again (with transparency) for comparison.
1023

1024 **Figure 4 Supplement 1: The effect of Clr6 I" in the *MAT ΔcenH* background.**
1025
1026 **A.** 2D-density hexbin plots with rug as in Figure 4C for *Δpng3* and WT control run on the same day in
1027 the *WT MAT* strain background.
1028
1029 **B.** 2D-density hexbin plots with rug as in Figure 4C for *Δpng3* and WT control run on the same day in
1030 the *MATΔREIII* strain background.
1031
1032 **C.** Scatter plot with rug for WT and Clr6 I" mutants in the *MAT ΔcenH* strain background. Cell are
1033 plotted as individual points versus summarized in 2D density hexbin plots for increased resolution.
1034 Points and rug lines are colored with partial transparency to assist with visualization of density changes.
1035
1036 **D.** ChIP-qPCR quantification of H3K9me2 signal in the *MAT ΔREIII* strain at the pericentromeric
1037 heterochromatin region. Error bars represent 1SD from three biological replicate isolates. Individual
1038 values are plotted for each isolate. SD; standard deviation.
1039

Figure 1

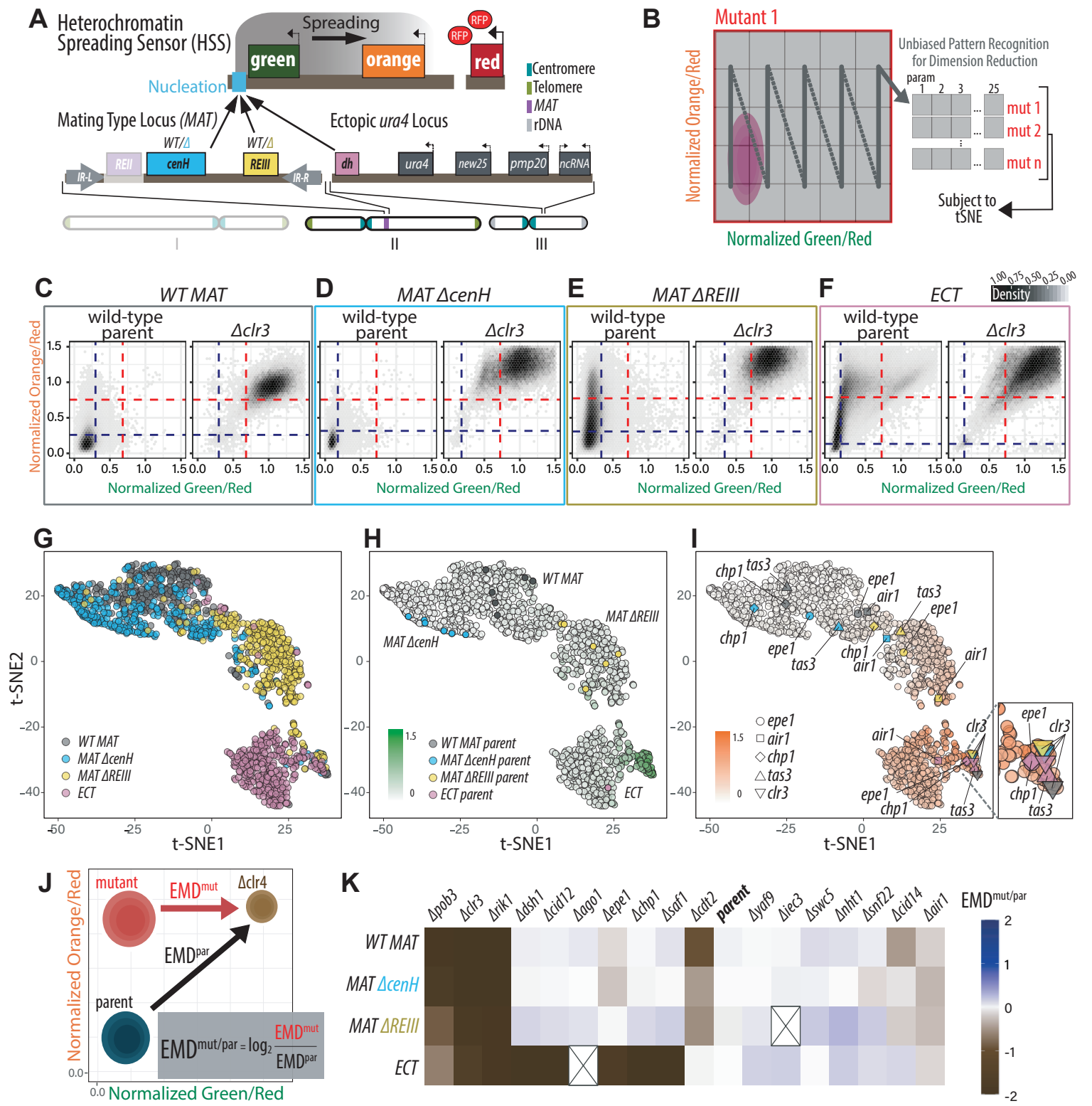
A
Heterochromatin Spreading Sensor (HSS)
Spreading
green
orange
red
RFP
Nucleation
Centromere
Telomere
MAT
rDNA
Mating Type Locus (MAT)
Ectopic ura4 Locus
WT/Δ
REII
cenH
REIII
IR-L
IR-R
dh
ura4
new25
pmp20
ncRNA
I
II
III
B
Mutant 1
Normalized Orange/Red
Normalized Green/Red
Unbiased Pattern Recognition for Dimension Reduction
param
mut 1
mut 2
mut n
Subject to tSNE
C
WT MAT
D
MAT ΔcenH
E
MAT ΔREIII
F
ECT
Density
wild-type parent
Δclr3
Normalized Orange/Red
Normalized Green/Red
G
H
I
t-SNE1
t-SNE2
WT MAT
MAT ΔcenH
MAT ΔREIII
ECT
WT MAT parent
MAT ΔcenH parent
MAT ΔREIII parent
ECT parent
epe1
air1
chp1
tas3
clr3
J
mutant
EMDmut
Δclr4
EMDpar
parent
EMDmut/par = log2 EMDmut / EMDpar
Normalized Orange/Red
Normalized Green/Red
K
Δpob3
Δclr3
Δrik1
Δdsh1
Δcid12
Δago1
Δepe1
Δchp1
Δsaf1
Δcdt2
parent
Δyaf9
Δiec3
Δswc5
Δnht1
Δsnf22
Δcid14
Δair1
WT MAT
MAT ΔcenH
MAT ΔREIII
ECT
EMDmut/par

Figure 2

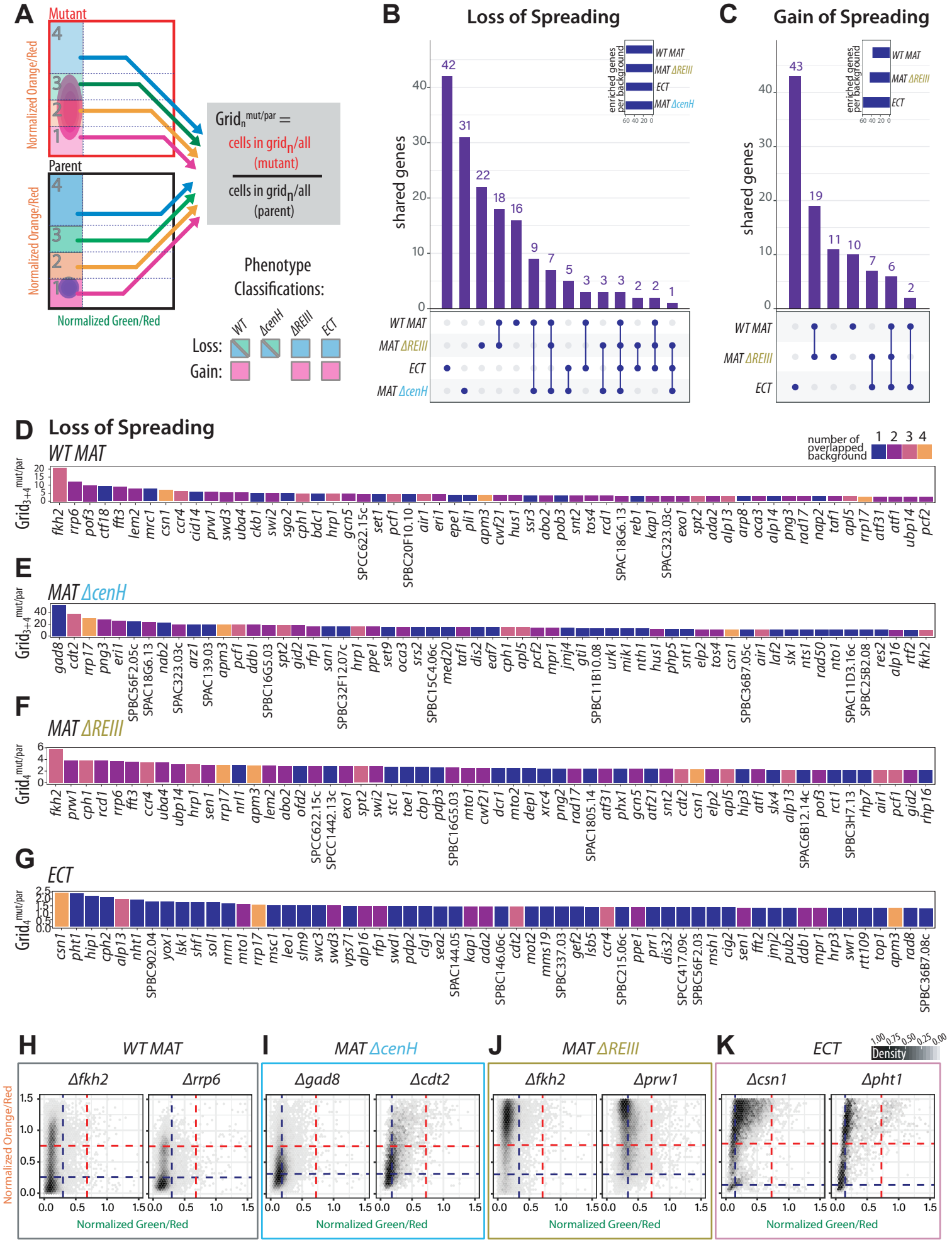
A
Mutant
Parent
Normalized Orange/Red
Normalized Green/Red
Grid$_n^{mut/par}$ = cells in grid$_n$/all (mutant) / cells in grid$_n$/all (parent)
Phenotype Classifications:
WT
ΔcenH
ΔREIII
ECT
Loss:
Gain:
B
Loss of Spreading
shared genes
enriched genes per background
WT MAT
MAT ΔREIII
ECT
MAT ΔcenH
C
Gain of Spreading
D
Loss of Spreading
WT MAT
number of overlapped background
E
MAT ΔcenH
F
MAT ΔREIII
G
ECT
H
WT MAT
Δfkh2
Δrrp6
I
MAT ΔcenH
Δgad8
Δcdt2
J
MAT ΔREIII
Δfkh2
Δprw1
K
ECT
Δcsn1
Δpht1
Density
Normalized Orange/Red
Normalized Green/Red

Figure 3

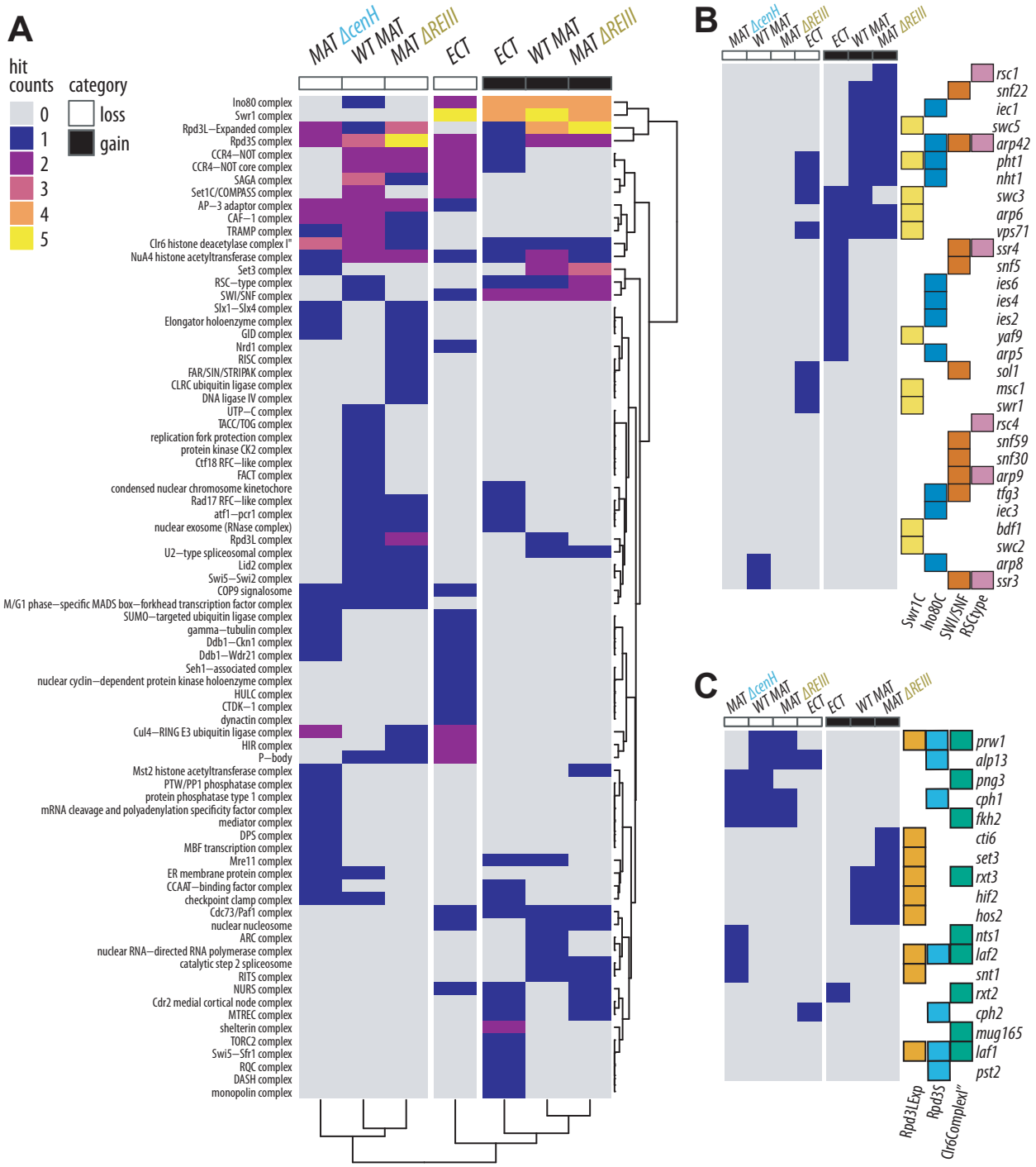
A
hit counts
0
1
2
3
4
5
category
loss
gain
MAT ΔcenH
WT MAT
MAT ΔREIII
ECT
ECT
WT MAT
MAT ΔREIII
Ino80 complex
Swr1 complex
Rpd3L–Expanded complex
Rpd3S complex
CCR4–NOT complex
CCR4–NOT core complex
SAGA complex
Set1C/COMPASS complex
AP–3 adaptor complex
CAF–1 complex
TRAMP complex
Clr6 histone deacetylase complex I"
NuA4 histone acetyltransferase complex
Set3 complex
RSC–type complex
SWI/SNF complex
Slx1–Slx4 complex
Elongator holoenzyme complex
GID complex
Nrd1 complex
RISC complex
FAR/SIN/STRIPAK complex
CLRC ubiquitin ligase complex
DNA ligase IV complex
UTP–C complex
TACC/TOG complex
replication fork protection complex
protein kinase CK2 complex
Ctf18 RFC–like complex
FACT complex
condensed nuclear chromosome kinetochore
Rad17 RFC–like complex
atf1–pcr1 complex
nuclear exosome (RNase complex)
Rpd3L complex
U2–type spliceosomal complex
Lid2 complex
Swi5–Swi2 complex
COP9 signalosome
M/G1 phase–specific MADS box–forkhead transcription factor complex
SUMO–targeted ubiquitin ligase complex
gamma–tubulin complex
Ddb1–Ckn1 complex
Ddb1–Wdr21 complex
Seh1–associated complex
nuclear cyclin–dependent protein kinase holoenzyme complex
HULC complex
CTDK–1 complex
dynactin complex
Cul4–RING E3 ubiquitin ligase complex
HIR complex
P–body
Mst2 histone acetyltransferase complex
PTW/PP1 phosphatase complex
protein phosphatase type 1 complex
mRNA cleavage and polyadenylation specificity factor complex
mediator complex
DPS complex
MBF transcription complex
Mre11 complex
ER membrane protein complex
CCAAT–binding factor complex
checkpoint clamp complex
Cdc73/Paf1 complex
nuclear nucleosome
ARC complex
nuclear RNA–directed RNA polymerase complex
catalytic step 2 spliceosome
RITS complex
NURS complex
Cdr2 medial cortical node complex
MTREC complex
shelterin complex
TORC2 complex
Swi5–Sfr1 complex
RQC complex
DASH complex
monopolin complex
B
rsc1
snf22
iec1
swc5
arp42
pht1
nht1
swc3
arp6
vps71
ssr4
snf5
ies6
ies4
ies2
yaf9
arp5
sol1
msc1
swr1
rsc4
snf59
snf30
arp9
tfg3
iec3
bdf1
swc2
arp8
ssr3
Swr1C
Ino80C
SWI/SNF
RSCtype
C
prw1
alp13
png3
cph1
fkh2
cti6
set3
rxt3
hif2
hos2
nts1
laf2
snt1
rxt2
cph2
mug165
laf1
pst2
Rpd3LExp
Rpd3S
Clr6Complex I"

Figure 4

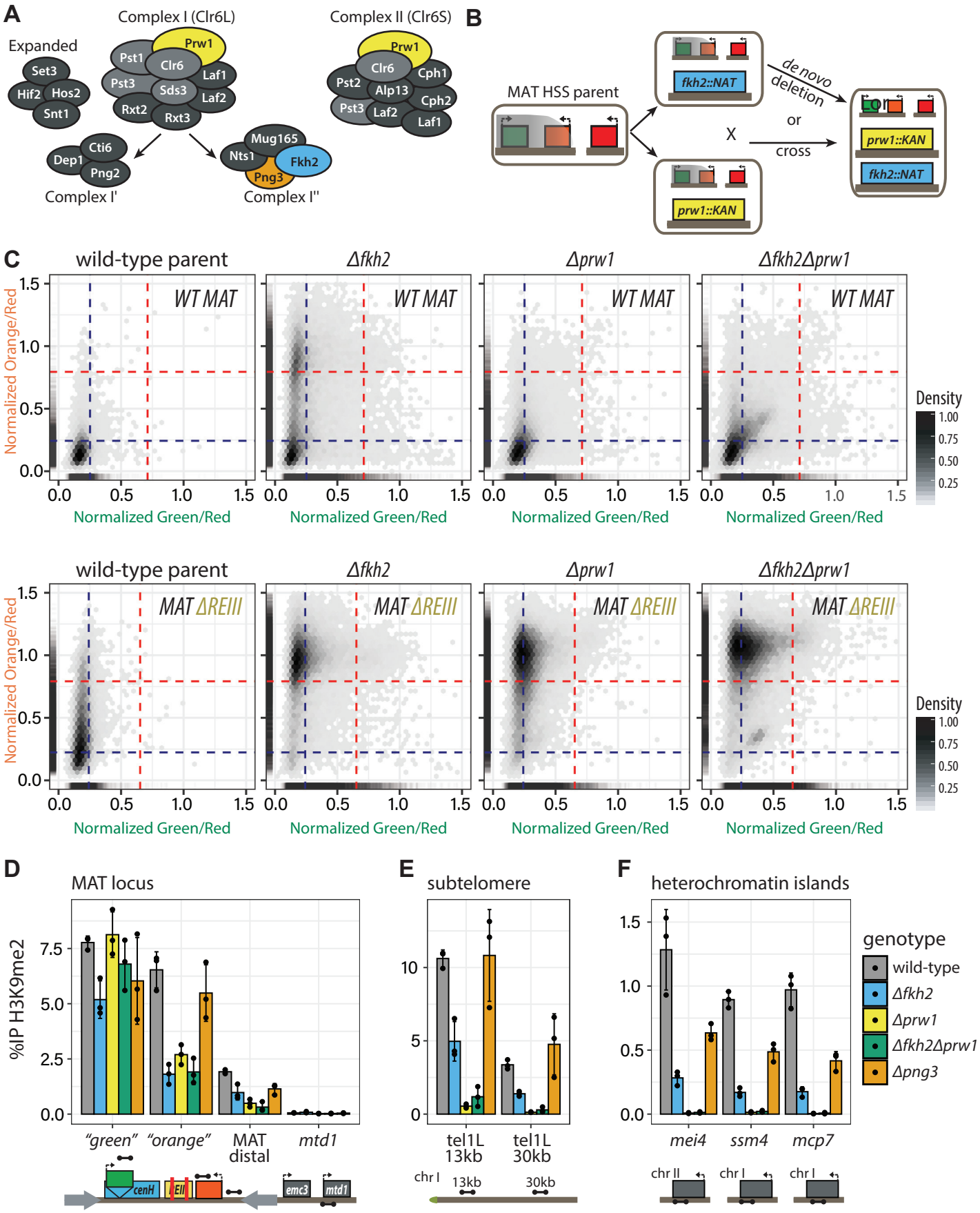
A
Complex I (Clr6L)
Complex II (Clr6S)
Expanded
Set3
Hif2
Hos2
Snt1
Prw1
Pst1
Clr6
Laf1
Pst3
Sds3
Laf2
Rxt2
Rxt3
Cti6
Dep1
Png2
Complex I'
Mug165
Nts1
Fkh2
Png3
Complex I''
Prw1
Clr6
Cph1
Pst2
Alp13
Cph2
Pst3
Laf2
Laf1
B
MAT HSS parent
fkh2::NAT
prw1::KAN
de novo deletion
or
X
cross
prw1::KAN
fkh2::NAT
C
wild-type parent
Δfkh2
Δprw1
Δfkh2Δprw1
WT MAT
Normalized Orange/Red
Normalized Green/Red
Density
1.00
0.75
0.50
0.25
MAT ΔREIII
D
MAT locus
%IP H3K9me2
"green"
"orange"
MAT distal
mtd1
cenH
EII
emc3
mtd1
E
subtelomere
tel1L 13kb
tel1L 30kb
chr I
13kb
30kb
F
heterochromatin islands
mei4
ssm4
mcp7
chr II
chr I
chr I
genotype
wild-type
Δfkh2
Δprw1
Δfkh2Δprw1
Δpng3

Figure 1 - Supplement 1

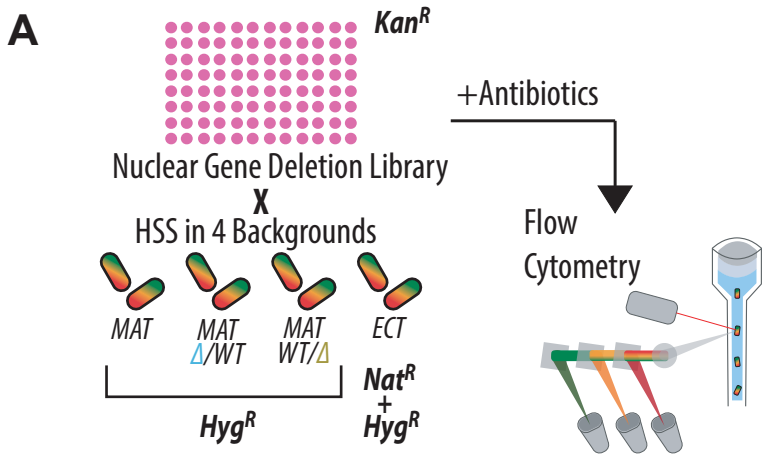

Figure 1 - Supplement 2

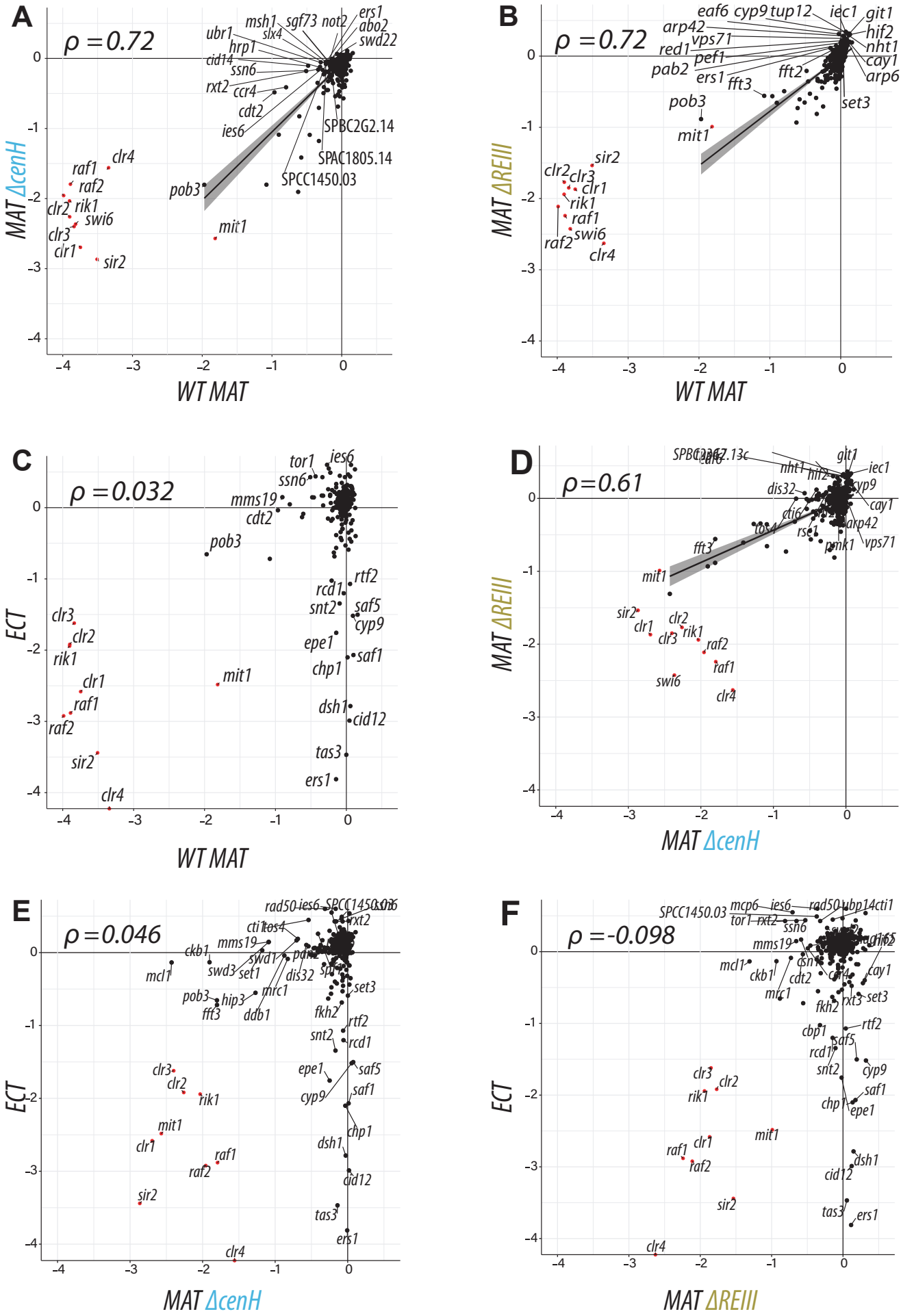

Figure 2 - Supplement 1

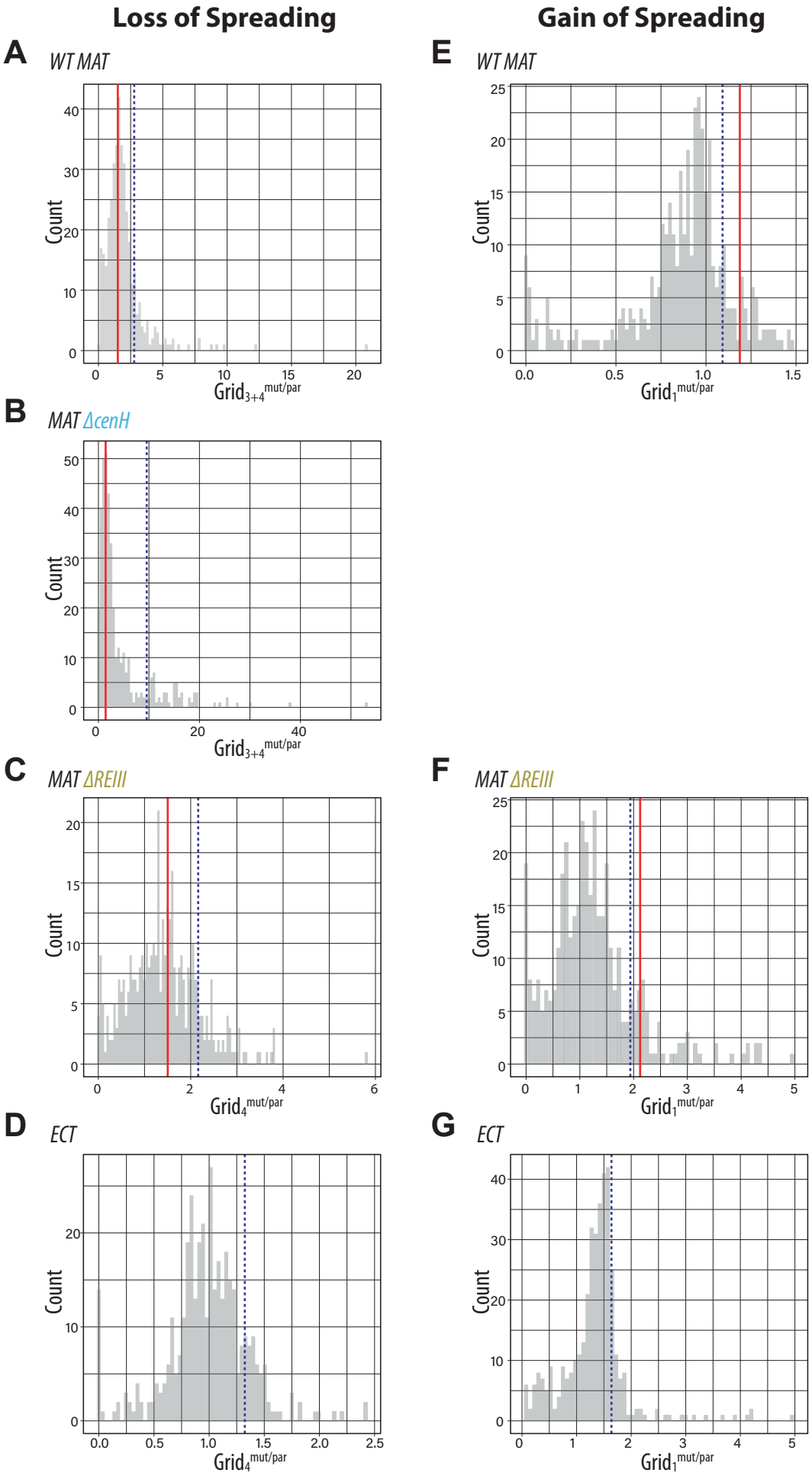

Figure 2 - Supplement 2

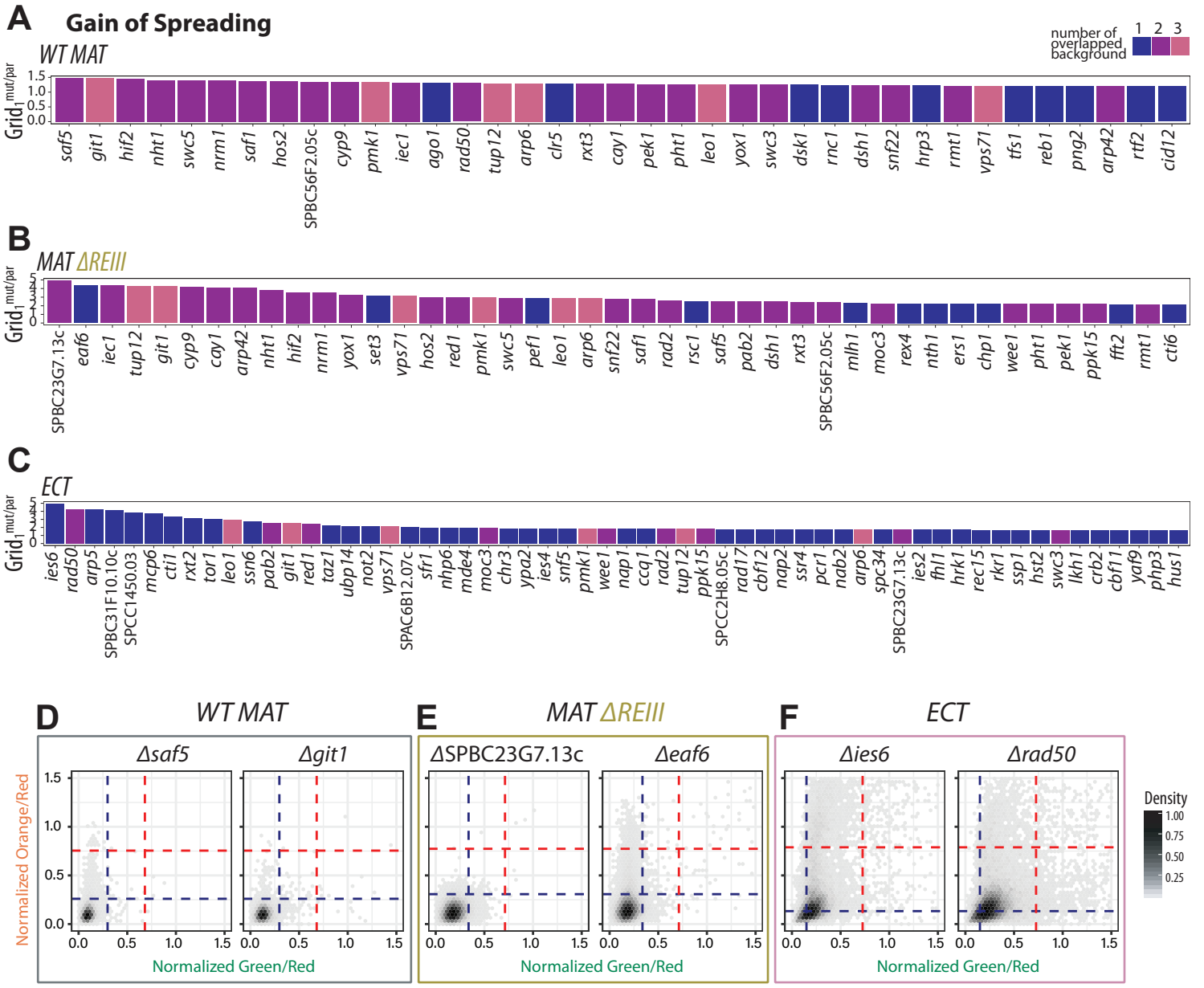

Figure 3 - Supplement 1

A *MAT ΔREIII* - Chromatin Remodelers

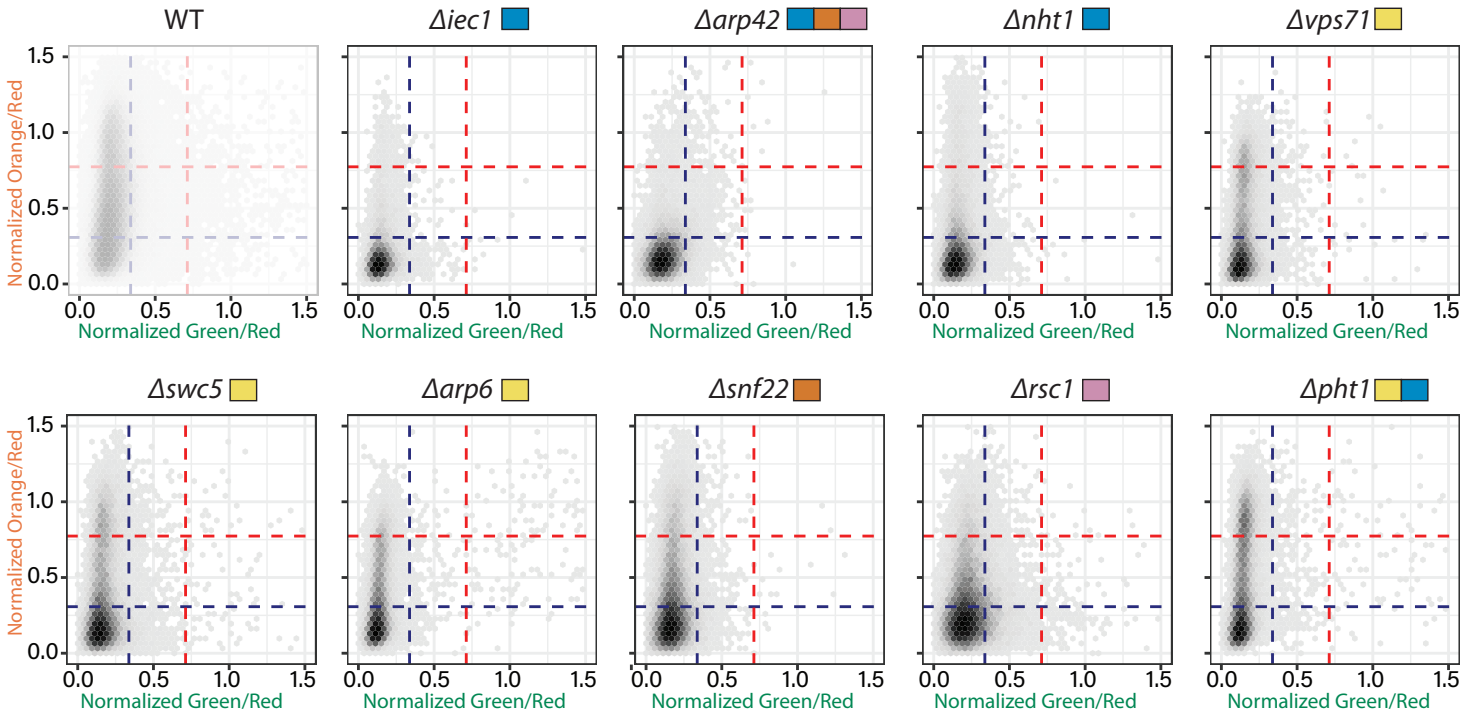

B *ECT* - Chromatin Remodelers

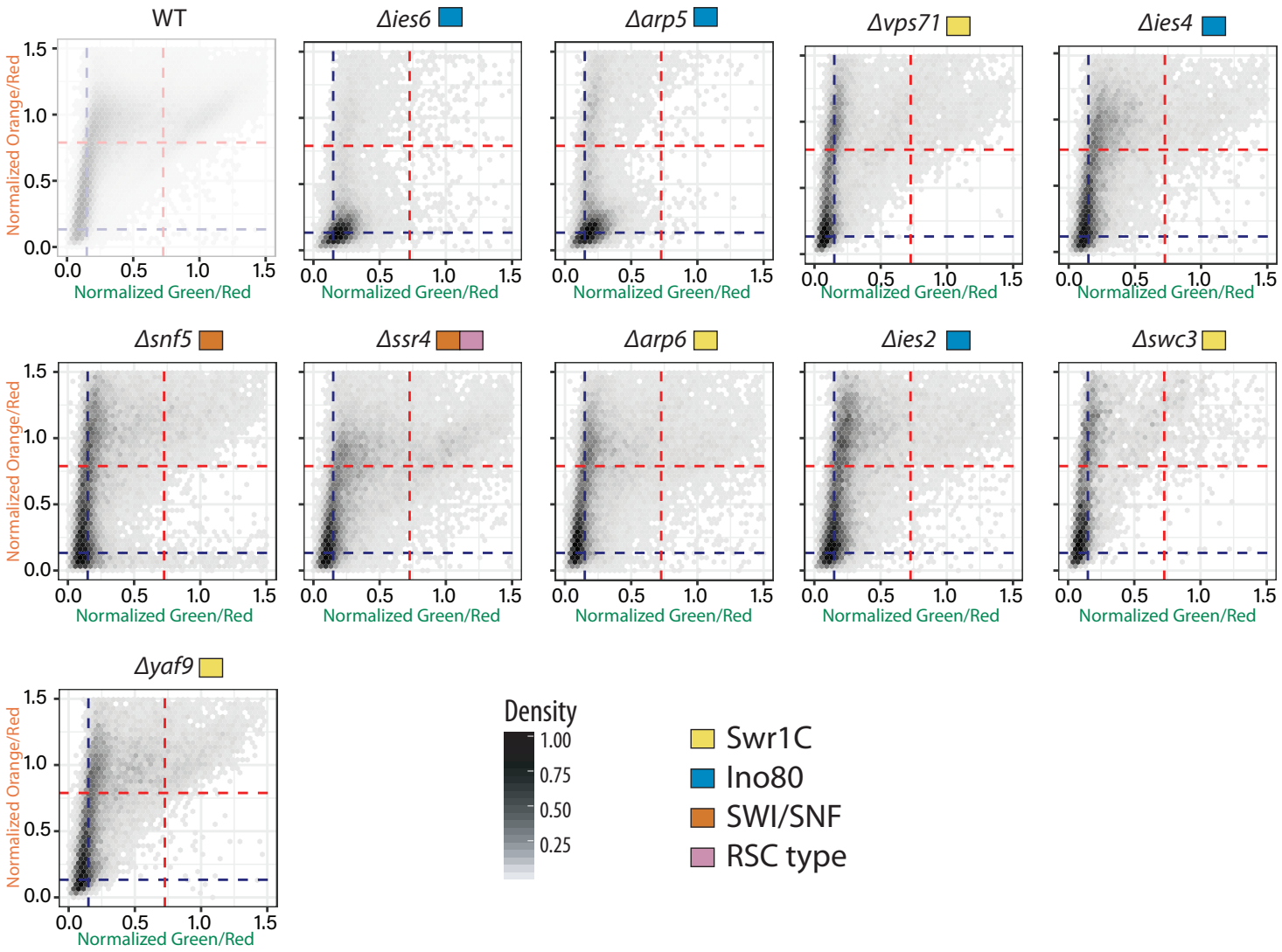

Figure 3 - Supplement 2

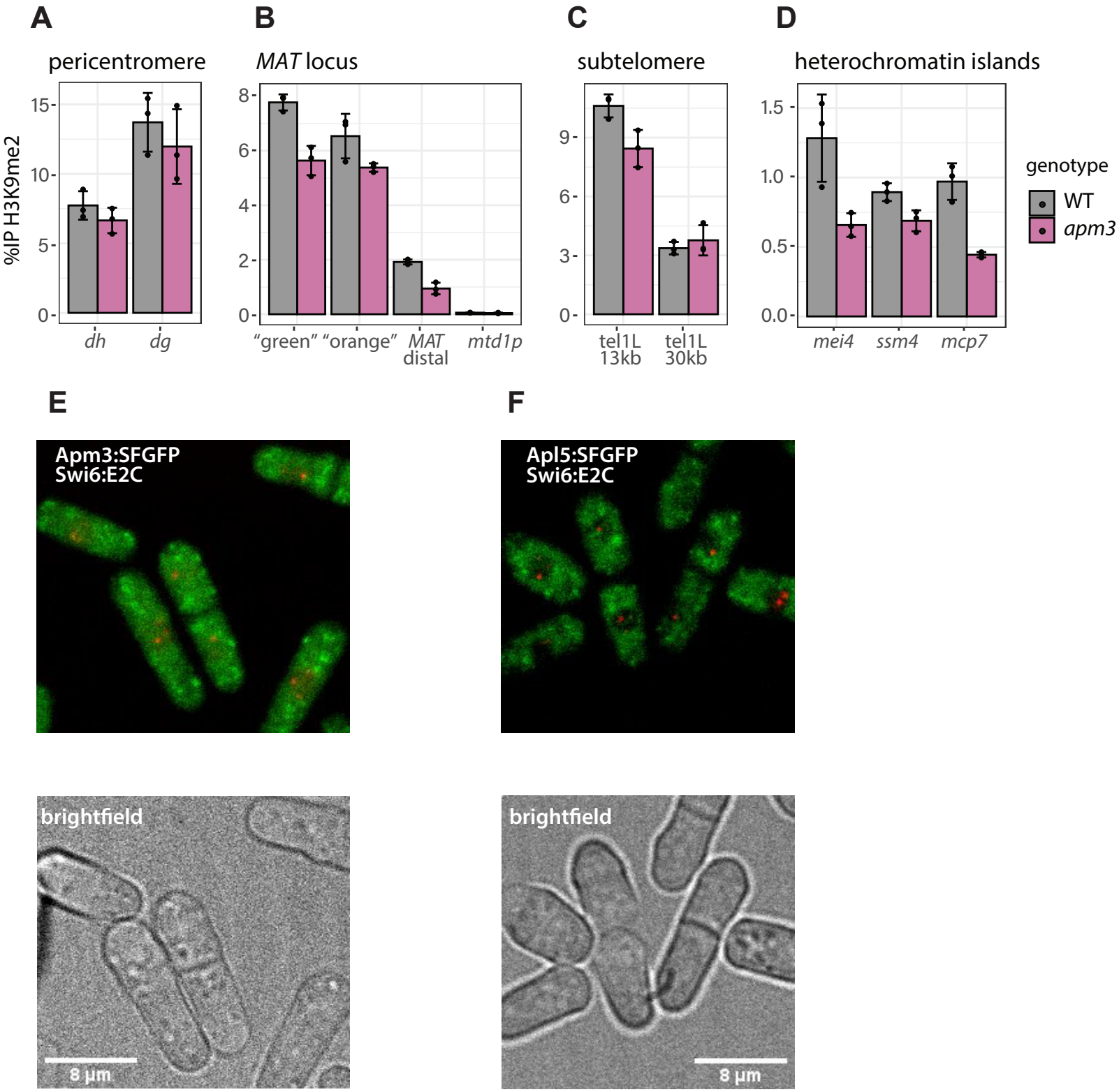

Figure 3 - Supplement 3

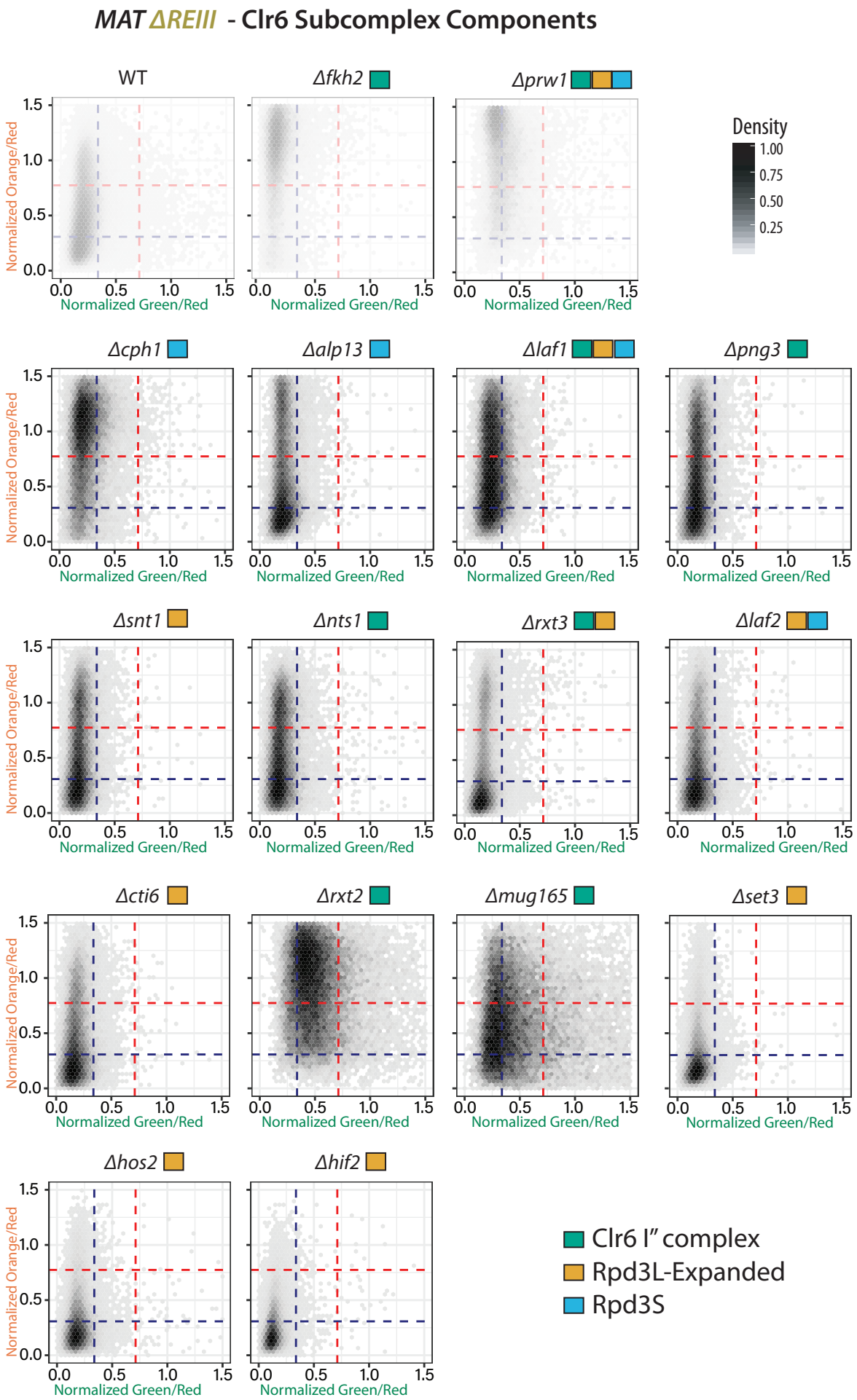

Figure 4 Supplement 1

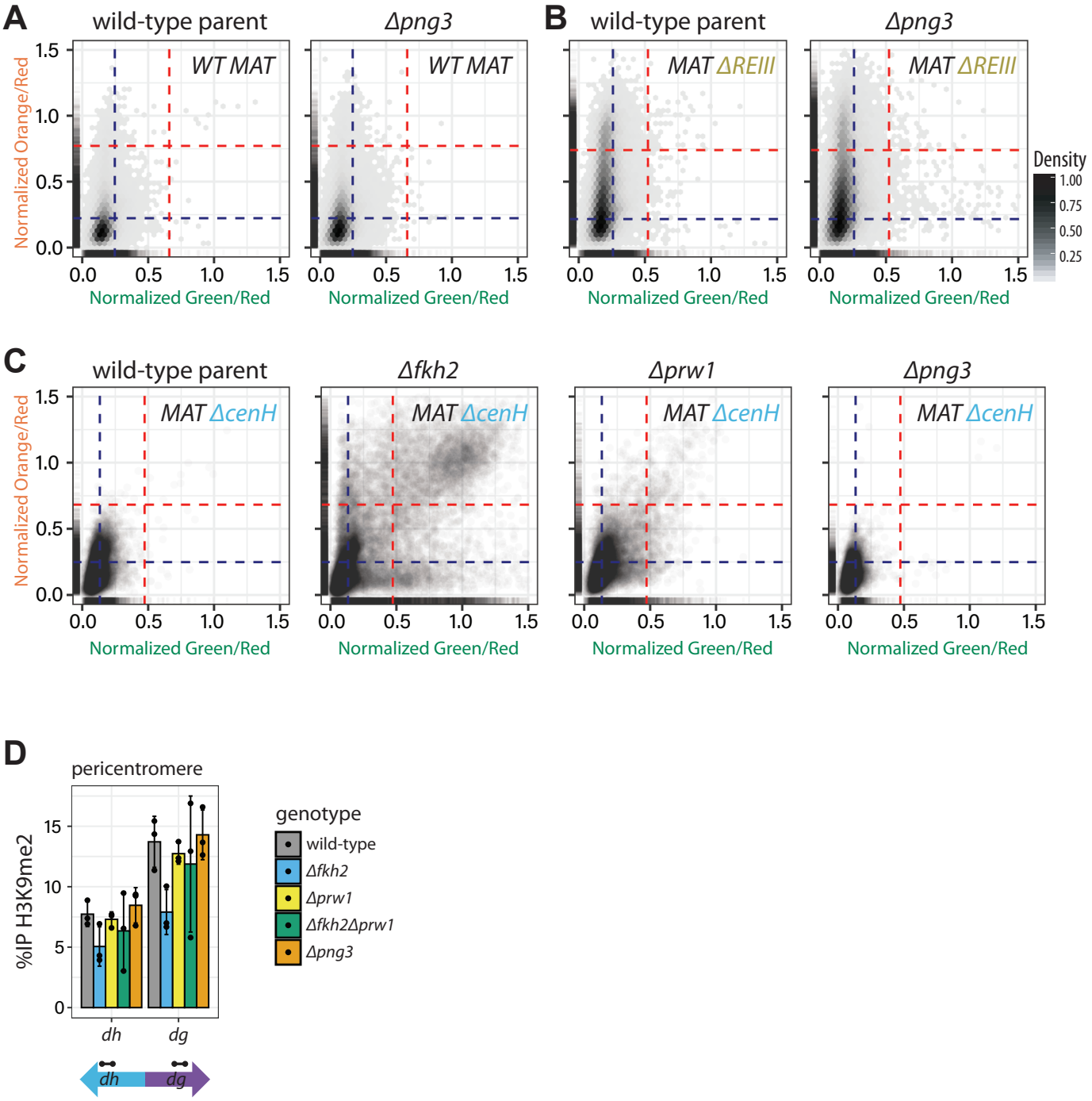

Table 1: Nuclear function deletion library

Table 1: Nuclear function gene deletion library

	Systematic ID	Symbol	Description
1	SPAC1002.05c	jmj2	histone demethylase Jmj2
2	SPAC1006.03c	red1	RNA elimination defective protein Red1
3	SPAC1039.05c	klf1	transcription factor, zf-fungal binuclear cluster type Klf1
4	SPAC1071.02	mms19	CIA machinery protein Mms19
5	SPAC1071.06	arp9	SWI/SNF and RSC complex subunit Arp9
6	SPAC10F6.08c	nht1	Ino80 complex HMG box subunit Nht1
7	SPAC10F6.11c	atg17	autophagy associated protein kinase activator Atg17
8	SPAC1142.03c	swi2	Swi5 complex subunit Swi2
9	SPAC1142.08	fhl1	forkhead transcription factor Fhl1
10	SPAC11D3.07c	toe4	transcription factor, zf-fungal binuclear cluster type(predicted)
11	SPAC11D3.16c		Schizosaccharomyces specific protein
12	SPAC11E3.01c	swr1	SNF2 family ATP-dependent DNA helicase Swr1
13	SPAC11H11.01	sst6	ESCRT I complex subunit Vps23
14	SPAC11H11.05c	fta6	Mis6-Sim4 complex Fta6
15	SPAC12B10.10	nod1	medial cortical node Gef2-related protein protein Nod1
16	SPAC12G12.13c	cid14	TRAMP complex poly(A) polymerase subunit Cid14
17	SPAC139.03	toe2	transcription factor, zf-fungal binuclear cluster type (predicted)
18	SPAC139.06	hat1	histone acetyltransferase Hat1
19	SPAC1399.05c	toe1	transcription factor, zf-fungal binuclear cluster type
20	SPAC13A11.04c	ubp8	SAGA complex ubiquitin C-terminal hydrolase Ubp8
21	SPAC13D6.02c	byr3	translational activator, zf-CCHC type zinc finger protein (predicted)
22	SPAC13G6.01c	rad8	ubiquitin-protein ligase E3/ ATP-dependent DNA helicase Rad8
23	SPAC144.02	iec1	Ino80 complex subunit Iec1
24	SPAC144.05		DNA-dependent ATPase/ ubiquitin-protein ligase E3 (predicted)
25	SPAC144.06	apl5	AP-3 adaptor complex subunit Apl5 (predicted)
26	SPAC144.14	klp8	kinesin-like protein Klp8
27	SPAC14C4.06c	nab2	poly(A) binding protein Nab2 (predicted)
28	SPAC14C4.12c	laf1	Clr6 L associated factor 1 Laf1
29	SPAC14C4.13	rad17	RFC related checkpoint protein Rad17
30	SPAC1556.01c	rad50	DNA repair protein Rad50
31	SPAC15A10.11	ubr11	UBR ubiquitin-protein ligase E3 Ubr11
32	SPAC15A10.15	sgo2	inner centromere protein, shugoshin Sgo2
33	SPAC1610.01	saf5	splicing factor Saf5
34	SPAC1610.02c	mrpl1	mitochondrial ribosomal protein subunit L1 (predicted)
35	SPAC1687.05	pli1	SUMO E3 ligase Pli1
36	SPAC1687.09	irs4	autophagy/CVT pathway ENTH/VHS domain protein Irs4 (predicted)
37	SPAC16A10.03c		ubiquitin-protein ligase E3 involved in vesicle docking Pep5/Vps11-like (predicted)
38	SPAC16A10.07c	taz1	shelterin complex subunit Taz1
39	SPAC16C9.04c	mot2	CCR4-Not complex ubiquitin-protein ligase E3 subunit Mot2
40	SPAC16C9.05	cph1	Clr6 histone deacetylase associated PHD protein-1 Cph1
41	SPAC16E8.12c	png3	ING family homolog Png3 (predicted)
42	SPAC1751.01c	gti1	gluconate transmembrane transporter inducer Gti1
43	SPAC1782.05	ypa2	protein phosphatase type 2A regulator, PTPA family Ypa2
44	SPAC1782.08c	rex3	exonuclease Rex3 (predicted)
45	SPAC1782.09c	clp1	Cdc14-related protein phosphatase Clp1/Flp1
46	SPAC1783.05	hrp1	ATP-dependent DNA helicase Hrp1
47	SPAC17A2.12	rrp1	ATP-dependent DNA helicase/ ubiquitin-protein ligase E3 (predicted)
48	SPAC17G8.05	med20	mediator complex subunit Med20
49	SPAC17G8.07	yaf9	YEATS family histone acetyltransferase subunit Yaf9
50	SPAC17G8.09	shg1	Set1C complex subunit Shg1
51	SPAC17G8.10c	dma1	mitotic spindle checkpoint ubiquitin ligase Dma1
52	SPAC17G8.13c	mst2	histone acetyltransferase Mst2
53	SPAC17H9.10c	ddb1	Cul4-RING E3 adaptor Ddb1
54	SPAC17H9.19c	cdt2	WD repeat protein Cdt2
55	SPAC1805.14		Schizosaccharomyces specific protein
56	SPAC1805.15c	pub2	HECT-type ubiquitin-protein ligase E3 Pub2
57	SPAC1851.03	ckb1	CK2 family regulatory subunit Ckb1
58	SPAC18G6.02c	chp1	heterochromatin (HP1) family chromodomain protein Chp1
59	SPAC18G6.10	lem2	LEM domain nuclear inner membrane protein Heh1/Lem2
60	SPAC18G6.13		Schizosaccharomyces specific protein
61	SPAC1952.05	gcn5	SAGA complex histone acetyltransferase catalytic subunit Gcn5
62	SPAC19A8.10	rfp1	SUMO-targeted ubiquitin-protein ligase subunit Rfp1
63	SPAC19D5.06c	din1	RNA pyrophosphohydrolase Din1
64	SPAC19D5.11c	ctf8	Ctf18 RFC-like complex subunit Ctf8
65	SPAC19E9.02	fin1	serine/threonine protein kinase, NIMA related Fin1
66	SPAC19G12.13c	poz1	shelterin complex subunit Poz1
67	SPAC19G12.17	erh1	enhancer of rudimentary homolog Erh1
68	SPAC1B3.17	clr2	chromatin silencing protein Clr2
69	SPAC1D4.09c	rtf2	replication termination factor Rtf2
70	SPAC1D4.11c	lkh1	dual specificity protein kinase Lkh1
71	SPAC1F3.01	rrp6	exosome 3'-5' exoribonuclease subunit Rrp6
72	SPAC1F3.06c	spo15	mitotic and mieotic spindle pole body protein Spo15

73	SPAC1F7.01c	spt6	nucleosome remodeling protein Spt6
74	SPAC20G4.04c	hus1	checkpoint clamp complex protein Hus1
75	SPAC20G8.08c	fft1	SMARCAD1 family ATP-dependent DNA helicase Fft1 (predicted)
76	SPAC20H4.03c	tfs1	general transcription elongation factor TFIIS
77	SPAC20H4.10	ufd2	ubiquitin-protein ligase E4 Ufd2 (predicted)
78	SPAC21E11.03c	pcr1	transcription factor Pcr1
79	SPAC21E11.05c	cyp8	cyclophilin family peptidyl-prolyl cis-trans isomerase Cyp8
80	SPAC222.04c	ies6	Ino80 complex subunit Ies6
81	SPAC222.15	meu13	Tat binding protein 1(TBP-1)-interacting protein (TBPIP) homolog (predicted)
82	SPAC22A12.01c	pso2	DNA 5' exonuclease (predicted)
83	SPAC22E12.11c	set3	histone lysine methyltransferase Set3
84	SPAC22E12.19	snt1	Set3 complex subunit Snt1
85	SPAC22F3.02	atf31	transcription factor Atf31
86	SPAC22F3.09c	res2	MBF transcription factor complex subunit Res2
87	SPAC22F8.12c	shf1	small histone ubiquitination factor Shf1
88	SPAC22H12.02	tfg3	TFIID, TFIIF, Ino80, SWI/SNF, and NuA3 complex subunit Tfg3
89	SPAC23A1.07		ubiquitin-protein ligase E3 (predicted)
90	SPAC23C11.08	php3	CCAAT-binding factor complex subunit Php3
91	SPAC23C11.15	pst2	Clr6 histone deacetylase complex subunit Pst2
92	SPAC23C4.03	hrk1	haspin related kinase Hrk1
93	SPAC23D3.01	pdp3	PWWP domain protein, involved in chromatin remodeling (predicted)
94	SPAC23D3.09	arp42	SWI/SNF and RSC complex subunit Arp42
95	SPAC23E2.01	fep1	iron-sensing transcription factor Fep1
96	SPAC23E2.03c	ste7	arrestin family meiotic suppressor protein Ste7
97	SPAC23G3.04	ies4	Ino80 complex subunit Ies4
98	SPAC23G3.07c	snf30	SWI/SNF complex subunit Snf30
99	SPAC23G3.08c	ubp7	ubiquitin C-terminal hydrolase Ubp7
100	SPAC23G3.10c	ssr3	SWI/SNF and RSC complex subunit Ssr3
101	SPAC23H3.05c	swd1	Set1C complex subunit Swd1
102	SPAC23H4.12	alp13	MRG family Clr6 histone deacetylase complex subunit Alp13
103	SPAC24B11.10c	cfh1	SEL1/TPR repeat protein Cfh1 (predicted)
104	SPAC25A8.01c	fft3	SMARCAD1 family ATP-dependent DNA helicase Fft3
105	SPAC25H1.02	jmj1	histone demethylase Jmj1 (predicted)
106	SPAC26H5.03	pcf2	CAF assembly factor (CAF-1) complex subunit B, Pcf2
107	SPAC29A4.09		rRNA exonuclease Rrp17 (predicted)
108	SPAC29A4.18	prw1	Clr6 histone deacetylase complex subunit Prw1
109	SPAC29B12.02c	set2	histone lysine H3-K36 methyltransferase Set2
110	SPAC29B12.03	spd1	ribonucleotide reductase (RNR) inhibitor
111	SPAC29B12.06c	rcd1	CCR4-Not complex RNA-binding protein subunit Rcd1
112	SPAC29B12.08	clr5	Clr5 protein
113	SPAC2C4.07c	dis32	3'-5'-exoribonuclease activity Dis3L2
114	SPAC2F3.15	lsk1	P-TEFb-associated cyclin-dependent protein kinase Lsk1
115	SPAC2F3.16		ubiquitin-protein ligase E3, implicated in DNA repair (predicted)
116	SPAC2F7.07c	cph2	Clr6 histone deacetylase associated PHD protein Cph2
117	SPAC2F7.08c	snf5	SWI/SNF complex subunit Snf5
118	SPAC2G11.05c	rim20	BRO1 domain protein Rim20
119	SPAC2G11.10c	uba42	thiosulfate sulfurtransferase, URM1 activating enzyme E1-type Uba42 (predicted)
120	SPAC30D11.07	nth1	DNA endonuclease III
121	SPAC31A2.09c	apm4	AP-2 adaptor complex mu subunit Apm4 (predicted)
122	SPAC31A2.16	gef2	RhoGEF Gef2
123	SPAC31G5.09c	spk1	MAP kinase Spk1
124	SPAC31G5.19	abo1	ATPase with bromodomain protein
125	SPAC323.03c		Schizosaccharomyces specific protein
126	SPAC328.05	hrb1	RNA-binding protein involved in export of mRNAs Hrb1 (predicted)
127	SPAC32A11.03c	phx1	stationary phase-specific homeobox transcription factor Phx1
128	SPAC343.04c	gid7	GID complex subunit Gid7 (predicted)
129	SPAC343.11c	msc1	Swr1 complex subunit Msc1
130	SPAC343.18	rfp2	SUMO-targeted ubiquitin-protein ligase subunit Rfp2
131	SPAC3A11.05c	kms1	meiotic spindle pole body KASH domain protein Kms1
132	SPAC3C7.08c	elf1	AAA family ATPase Elf1
133	SPAC3F10.10c	map3	pheromone M-factor receptor Map3
134	SPAC3F10.12c		transcription factor (predicted)
135	SPAC3G6.01	hrp3	ATP-dependent DNA helicase Hrp3
136	SPAC3G6.06c	rad2	FEN-1 endonuclease Rad2
137	SPAC3G6.11	chl1	ATP-dependent DNA helicase Chl1 (predicted)
138	SPAC3G9.07c	hos2	histone deacetylase (class I) Hos2
139	SPAC3H1.11	hsr1	transcription factor Hsr1
140	SPAC3H1.12c	snt2	Lid2 complex PHD finger subunit Snt2
141	SPAC3H8.08c		transcription factor (predicted)
142	SPAC4A8.09c	cwf21	complexed with Cdc5 protein Cwf21
143	SPAC4F8.11	sea2	SEA complex WD repeat subunit Sea2 (predicted)
144	SPAC4G9.06c	chz1	histone H2A-H2B dimer chaperone Chz1 (predicted)
145	SPAC4H3.02c	swc3	Swr1 complex subunit Swc3
146	SPAC4H3.05	srs2	ATP-dependent DNA helicase, UvrD subfamily

147	SPAC56F8.16	esc1	transcription factor Esc1 (predicted)
148	SPAC57A10.09c	nhp6	High-mobility group non-histone chromatin protein (predicted)
149	SPAC5D6.02c	mug165	Clr6 histone deacetylase complex subunit Mug165
150	SPAC5D6.08c	mes1	meiotic APC inhibitor Mes1
151	SPAC630.14c	tup12	transcriptional corepressor Tup12
152	SPAC631.02	bdf2	BET family double bromodomain protein Bdf2
153	SPAC637.09	rex1	3'-5'- exoribonuclease Rex1 (predicted)
154	SPAC644.14c	rad51	RecA family recombinase Rad51/Rhp51
155	SPAC664.01c	swi6	heterochromatin (HP1) family chromodomain protein Swi6
156	SPAC664.02c	arp8	Ino80 complex actin-like protein Arp8
157	SPAC664.07c	rad9	checkpoint clamp complex protein Rad9
158	SPAC664.15	caf4	CCR4-Not complex subunit Caf4/Mdv1 (predicted)
159	SPAC688.06c	slx4	structure-specific endonuclease subunit Slx4
160	SPAC694.06c	mrc1	claspin, Mrc1
161	SPAC6B12.05c	ies2	Ino80 complex subunit Ies2
162	SPAC6B12.07c		ubiquitin-protein ligase E3 with SPX domain, human LORNRF1 ortholog (predicted)
163	SPAC6B12.14c		conserved fungal protein
164	SPAC6B12.16	meu26	DUF4451 family conserved fungal protein
165	SPAC6F12.09	rdp1	RNA-directed RNA polymerase Rdp1
166	SPAC6F6.09	eaf6	Mst2/NuA4 histone acetyltransferase complex subunit Eaf6
167	SPAC6G9.03c	mug183	histone H3.3 H4 heterotetramer chaperone Rtt106-like (predicted)
168	SPAC6G9.10c	sen1	ATP-dependent 5' to 3' DNA/RNA helicase Sen1
169	SPAC6G9.16c	xrc4	XRCC4 nonhomologous end joining factor Xrc4
170	SPAC7D4.04	atg11	autophagy associated protein Atg11
171	SPAC7D4.14c	iss10	NURS complex subunit Iss10
172	SPAC821.07c	moc3	transcription factor Moc3
173	SPAC823.03	ppk15	serine/threonine protein kinase Ppk15 (predicted)
174	SPAC824.04	swd22	mRNA cleavage and polyadenylation specificity factor complex, WD repeat protein Swd22
175	SPAC890.07c	rmt1	type I protein arginine N-methyltransferase Rmt1
176	SPAC8C9.14	prr1	transcription factor Prr1
177	SPAC8C9.17c	spc34	DASH complex subunit Spc34
178	SPAC8F11.03	msh3	MutS protein homolog 3
179	SPAC9E9.08	rad26	ATRIP, ATR checkpoint kinase regulatory subunit Rad26
180	SPAC9E9.10c	cbh1	CENP-B homolog Cbh1
181	SPAP14E8.02	tos4	chromatin binding FHA domain protein Tos4 (predicted)
182	SPAP27G11.15	slx1	structure-specific endonuclease catalytic subunit Slx1
183	SPAP32A8.03c	bop1	ubiquitin-protein ligase E3, human RNF126 ortholog (predicted)
184	SPAP8A3.02c	ofd2	histone H2A dioxygenase Ofd2
185	SPAPB1E7.02c	mcl1	DNA polymerase alpha accessory factor Mcl1
186	SPAPB24D3.01	toe3	transcription factor (predicted)
187	SPAPB2B4.03	cig2	G1/S-specific B-type cyclin Cig2
188	SPBC1105.04c	cbp1	CENP-B homolog
189	SPBC119.08	pmk1	MAP kinase Pmk1
190	SPBC119.14	rti1	Rad22 homolog Rti1
191	SPBC1198.11c	reb1	RNA polymerase I transcription termination factor/ RNA polymerase II transcription factor Reb1
192	SPBC11B10.05c	rsp1	random septum position protein, DNAJ domain protein Rsp1
193	SPBC11B10.08		WW domain containing conserved fungal protein
194	SPBC11B10.10c	pht1	histone H2A variant H2A.Z, Pht1
195	SPBC1347.07	rex2	RNA exonuclease (predicted)
196	SPBC13E7.08c	leo1	RNA polymerase II associated Paf1 complex subunit Leo1
197	SPBC13G1.08c	ash2	Ash2-trithorax family protein
198	SPBC146.06c	fan1	DNA repair protein Fan1
199	SPBC14C8.17c	spt8	SAGA complex subunit Spt8
200	SPBC14F5.07	doa10	ER ubiquitin-protein ligase E3 Doa10 (predicted)
201	SPBC15C4.01c	oca3	TPR repeat protein Oca3/ ER membrane protein complex Ecm2 (predicted)
202	SPBC15C4.06c		ubiquitin-protein ligase E3 Meu34, human RNF13 family homolog, unknown biological role (predicted)
203	SPBC15D4.03	slm9	histone H3.3 H4 chaperone, hira family Slm9
204	SPBC1604.09c	rex4	exoribonuclease Rex4 (predicted)
205	SPBC1604.16c		RNA-binding protein, G-patch type, human GPANK1 ortholog
206	SPBC1685.08	cti6	histone deacetylase complex ubiquitin-like protein ligase subunit Cti6
207	SPBC16A3.07c	nrm1	MBF complex corepressor Nrm1
208	SPBC16A3.19	eaf7	histone acetyltransferase complex subunit Eaf7
209	SPBC16D10.07c	sir2	Sirtuin family histone deacetylase Sir2
210	SPBC16E9.11c	pub3	HECT-type ubiquitin-protein ligase E3 Pub3 (predicted)
211	SPBC16E9.12c	pab2	poly(A) binding protein Pab2
212	SPBC16G5.03	mrz1	ubiquitin-protein ligase E3/SUMO transferase, Topors, possibly associated with DNA damage (predicted)
213	SPBC16G5.15c	fkh2	forkhead transcription factor Fkh2
214	SPBC16G5.17		transcription factor, zf-fungal binuclear cluster type (predicted)
215	SPBC1703.04	mlh1	MutL family protein Mlh1 (predicted)
216	SPBC1703.14c	top1	DNA topoisomerase I
217	SPBC1709.11c	png2	ING family histone acetyltransferase complex PHD-type zinc finger subunit Png2
218	SPBC1711.14	rec15	meiotic recombination protein Rec15
219	SPBC1718.02	hop1	linear element associated protein Hop1
220	SPBC1734.06	rhp18	Rad18 homolog ubiquitin protein ligase E3, Rhp18

221	SPBC1734.15	rsc4	RSC complex subunit Rsc4
222	SPBC1773.16c		transcription factor, zf-fungal binuclear cluster type(predicted)
223	SPBC1778.10c	ppk21	serine/threonine protein kinase Ppk21 (predicted)
224	SPBC17D11.04c	nto1	histone acetyltransferase complex PHD finger subunit Nto1 (predicted)
225	SPBC17G9.05	rct1	cyclophilin family peptidyl-prolyl cis-trans isomerase, RRM-containing Rct1
226	SPBC18H10.06c	swd2	Set1C complex subunit Swd2.1
227	SPBC18H10.15	cdk11	serine/threonine protein kinase Cdk11
228	SPBC19C7.02	ubr1	N-end-recognizing protein, UBR ubiquitin-protein ligase E3 Ubr1
229	SPBC1A4.03c	top2	DNA topoisomerase II
230	SPBC1D7.03	clg1	cyclin-like protein involved in autophagy Clg1 (predicted)
231	SPBC1D7.04	mlo3	RNA binding protein Mlo3
232	SPBC20F10.05	nrl1	RNAi-mediated silencing protein, human NRDE2 ortholog Nrl1
233	SPBC20F10.10	psl1	cyclin pho85 family Psl1 (predicted)
234	SPBC215.03c	csn1	COP9/signalosome complex subunit Csn1
235	SPBC215.06c		nucleolar RNA-binding protein, human LYAR homolog, implicated in transcriptional regulation
236	SPBC215.07c	pdp2	PWWP domain protein Pdp2 (predicted)
237	SPBC216.05	rad3	ATR checkpoint kinase Rad3
238	SPBC216.06c	swi1	replication fork protection complex subunit Swi1
239	SPBC21B10.13c	yox1	MBF complex corepressor Yox1
240	SPBC21C3.02c	dep1	Sds3-like family protein Dep1
241	SPBC21C3.20c	git1	C2 domain protein Git1
242	SPBC21D10.09c	rkr1	RQC complex ubiquitin-protein ligase E3 Rkr1 (predicted)
243	SPBC21D10.10	bdc1	bromodomain protein Bdc1
244	SPBC23E6.02	rrp2	ATP-dependent DNA helicase/ ubiquitin-protein ligase E3 (predicted)
245	SPBC23E6.09	ssn6	transcriptional corepressor Ssn6
246	SPBC23G7.13c		plasma membrane urea transmembrane transporter (predicted)
247	SPBC24C6.05	sec28	coatomer epsilon subunit (predicted)
248	SPBC25B2.08		Schizosaccharomyces pombe specific protein
249	SPBC26H8.09c	snf59	SWI/SNF complex subunit Snf59
250	SPBC28E12.02		RNA-binding protein
251	SPBC28F2.07	sfr1	Swi five-dependent recombination mediator Sfr1
252	SPBC28F2.10c	ngg1	SAGA complex subunit Ngg1/Ada3
253	SPBC29A10.03c	pcf1	CAF assembly factor (CAF-1) complex large subunit Pcf1
254	SPBC29A10.05	exo1	exonuclease I Exo1
255	SPBC29A10.14	rec8	meiotic cohesin complex subunit Rec8
256	SPBC29A3.03c	gid2	GID complex ubiquitin-protein ligase E3 subunit Gid2/Rmd5 (predicted)
257	SPBC29A3.05	vps71	Swr1 complex subunit Vps71
258	SPBC29A3.13	pdp1	PWWP domain protein Pdp1
259	SPBC29B5.01	atf1	transcription factor, Atf-CREB family Atf1
260	SPBC2A9.04c	san1	sir antagonist, ubiquitin-protein ligase E3
261	SPBC2D10.11c	nap2	histone H2A-H2B chaperone Nap2
262	SPBC2D10.17	clr1	SHREC complex intermodule linker subunit Clr1
263	SPBC2F12.09c	atf21	transcription factor, Atf-CREB family Atf21
264	SPBC2F12.12c	cay1	cactin, spliceosome complex subunit
265	SPBC2G2.06c	apl1	AP-2 adaptor complex beta subunit Apl1 (predicted)
266	SPBC2G2.14	csi1	mitotic centromere-SPB clustering protein Csi1
267	SPBC2G5.02c	ckb2	CK2 family regulatory subunit Ckb2 (predicted)
268	SPBC30B4.04c	sol1	SWI/SNF complex subunit Sol1
269	SPBC30D10.10c	tor1	serine/threonine protein kinase Tor1
270	SPBC31F10.07	lsb5	actin cortical patch component Lsb5 (predicted)
271	SPBC31F10.10c	mub1	Armadillo-type fold protein, zf-MYND type zinc finger protein, Mub1-Rad6-Ubr2 ubiquitin ligase complex Mub1 (predicted)
272	SPBC31F10.13c	hip1	histone H3.3 H4 chaperone, hira family Hip1
273	SPBC31F10.14c	hip3	HIRA interacting protein Hip3
274	SPBC32F12.07c		membrane associated ubiquitin-protein ligase E3, MARCH family (predicted)
275	SPBC32H8.06	mug93	TPR repeat protein, meiotically spliced
276	SPBC337.03	rhn1	RNA polymerase II transcription termination factor homolog
277	SPBC342.05	crb2	DNA repair protein Rad9 homolog Crb2
278	SPBC342.06c	rtt109	RTT109 family histone lysine acetyltransferase
279	SPBC354.03	swd3	WD repeat protein Swd3
280	SPBC354.05c	sre2	membrane-tethered transcription factor Sre2
281	SPBC365.10	arp5	Ino80 complex actin-like protein Arp5
282	SPBC36B7.05c	pib1	endosomal and vacuolar ubiquitin-protein ligase E3/phosphatidylinositol(3)-phosphate binding protein Pib1
283	SPBC36B7.08c	ccp1	histone chaperone, CENP-A nucleosome disassembly Ccp1
284	SPBC3B8.02	php5	CCAAT-binding factor complex subunit Php5
285	SPBC3D6.04c	mad1	mitotic spindle checkpoint protein Mad1
286	SPBC3D6.09	dpb4	DNA polymerase epsilon subunit Dpb4
287	SPBC3H7.13	far10	SIP/FAR complex FHA domain subunit Far10/Csc1
288	SPBC4.05	mlo2	ubiquitin protein ligase E3 component human N-recognin 7 homolog Mlo2
289	SPBC428.06c	rxt2	histone deacetylase complex subunit Rxt2
290	SPBC428.08c	clr4	histone lysine H3 methyltransferase Clr4
291	SPBC4B4.03	rsc1	RSC complex subunit Rsc1
292	SPBC4C3.12	1-Sep	forkhead transcription factor Sep1
293	SPBC530.08		membrane-tethered transcription factor (predicted)
294	SPBC530.14c	dsk1	SR protein-specific kinase Dsk1

295	SPBC543.07	pek1	MAP kinase kinase Pek1
296	SPBC56F2.03	arp10	dynactin complex actin-like protein Arp10 (predicted)
297	SPBC56F2.05c		transcription factor (predicted)
298	SPBC582.04c	dsh1	RNAi protein, Dsh1
299	SPBC582.06c	mcp6	horsetail movement protein Hrs1/Mcp6
300	SPBC609.05	pob3	histone H2A-H2B chaperone, FACT complex subunit Pob3
301	SPBC651.11c	apm3	AP-3 adaptor complex subunit Apm3 (predicted)
302	SPBC660.06		WW domain containing conserved fungal protein
303	SPBC660.14	mik1	mitotic inhibitor kinase Mik1
304	SPBC6B1.04	mde4	microtubule-site clamp monopolin complex subunit Mde4
305	SPBC6B1.06c	ubp14	Lys48-specific deubiquitinase Ubp14
306	SPBC725.02	mpr1	histidine-containing response regulator phosphotransferase Mpr1
307	SPBC725.11c	php2	CCAAT-binding factor complex subunit Php2
308	SPBC776.02c	dis2	serine/threonine protein phosphatase PP1, Dis2
309	SPBC776.16	mis20	centromere protein Mis20/Eic2
310	SPBC800.03	clr3	histone deacetylase (class II) Clr3
311	SPBC83.03c	tas3	RITS complex subunit 3
312	SPBC902.02c	ctf18	Ctf18 RFC-like complex subunit Ctf18
313	SPBC902.04	rmn1	RNA-binding protein
314	SPBC902.06	mto2	gamma tubulin complex linker Mto2
315	SPBP16F5.03c	tra1	SAGA complex phosphatidylinositol pseudokinase Tra1
316	SPBP22H7.05c	abo2	ATPase with bromodomain protein (predicted)
317	SPBP23A10.05	ssr4	SWI/SNF and RSC complex subunit Ssr4
318	SPBP35G2.08c	air1	TRAMP complex zinc knuckle subunit Air1
319	SPBP35G2.10	mit1	SHREC complex ATP-dependent DNA helicase subunit Mit1
320	SPBP35G2.13c	swc2	Swr1 complex subunit Swc2
321	SPBP8B7.07c	set6	histone lysine methyltransferase Set6 (predicted)
322	SPBP8B7.23	rnf10	ubiquitin-protein ligase E3 (predicted)
323	SPBP8B7.28c	stc1	CLRC ubiquitin ligase complex linker protein, LIM-like Stc1
324	SPCC1020.12c	xap5	xap-5-like protein
325	SPCC11E10.08	rik1	CLRC ubiquitin ligase complex WD repeat protein Rik1
326	SPCC1223.13	cbf12	CBF1/Su(H)/LAG-1 family transcription factor Cbf12
327	SPCC1235.05c	fft2	SMARCAD1 family ATP-dependent DNA helicase Fft2 (predicted)
328	SPCC1235.09	hif2	Set3 complex subunit Hif2
329	SPCC1235.12c	mug146	Schizosaccharomyces specific protein Mug46
330	SPCC1259.04	iec3	Ino80 complex subunit Iec3
331	SPCC1259.07	rxt3	transcriptional regulatory protein Rxt3
332	SPCC126.02c	pku70	Ku domain protein Pku70
333	SPCC126.04c	sgf73	SAGA complex deubiquitinating submodule subunit Sgf73
334	SPCC126.07c	asr1	ubiquitin-protein ligase E3 Asr1 (predicted)
335	SPCC126.11c		RNA-binding protein, rrm type
336	SPCC126.13c	sap18	splicing factor Sap18 (predicted)
337	SPCC132.02	hst2	Sirtuin family histone deacetylase Hst2
338	SPCC1393.02c	spt2	non-specific DNA binding protein Spt2 (predicted)
339	SPCC1393.05	ers1	RNA-silencing factor Ers1
340	SPCC1442.13c	sqs2	R3H and G-patch domain protein Sqs2
341	SPCC1450.02	bdf1	Swr1 complex bromodomain subunit Bdf1
342	SPCC1450.03	utp502	ribonucleoprotein (RNP) complex Utp502 (predicted)
343	SPCC1494.03	arz1	human RAP1 GTPase-GDP dissociation stimulator ortholog, Zfs1 target number 1
344	SPCC162.11c	urk1	uridine kinase/uracil phosphoribosyltransferase (predicted)
345	SPCC1620.14c	snf22	ATP-dependent DNA helicase Snf22
346	SPCC1682.13	laf2	Clr6 associated factor 2, Laf2
347	SPCC16C4.11	pef1	Pho85/PhoA-like cyclin-dependent kinase Pef1
348	SPCC1739.03	hrr1	Helicase Required for RNAi-mediated heterochromatin assembly Hrr1
349	SPCC1739.05	set5	histone lysine methyltransferase Set5 (predicted)
350	SPCC1739.07	cti1	exosome C1D family subunit Cti1
351	SPCC1739.12	ppe1	serine/threonine protein phosphatase Ppe1
352	SPCC1753.03c	rec7	meiotic recombination protein Rec7
353	SPCC1840.04	pca1	metacaspase Pca1
354	SPCC188.07	ccq1	shelterin complex HEAT repeat subunit Ccq1
355	SPCC188.13c	dcr1	dicer
356	SPCC18B5.03	wee1	M phase inhibitor protein kinase Wee1
357	SPCC18B5.07c	nup61	nucleoporin Nup61
358	SPCC24B10.07	gad8	AGC family protein kinase Gad8
359	SPCC24B10.08c	ada2	SAGA complex subunit Ada2
360	SPCC24B10.14c	xlf1	XRCC4-like nonhomologous end joining factor, Cernunnon Xlf1/Nej1
361	SPCC24B10.19c	nts1	Clr6 histone deacetylase complex subunit Nts1
362	SPCC297.03	ssp1	Ca2+/calmodulin-dependent (CaMMK)-like protein kinase Ssp1
363	SPCC297.04c	set7	histone lysine H3-K37 methyltransferase Set7
364	SPCC2H8.05c	dbl1	double strand break localizing Dbl1
365	SPCC306.04c	set1	histone lysine H3-K4 methyltransferase Set1
366	SPCC31H12.08c	ccr4	CCR4-Not complex 3'-5'-exoribonuclease subunit Ccr4
367	SPCC330.01c	rhp16	Rad16 homolog ATP-dependent DNA helicase/ ubiquitin protein ligase E3 Rhp16
368	SPCC330.02	rhp7	Rad7 homolog Rhp7

369	SPCC338.16	pof3	F-box protein Pof3
370	SPCC364.02c	bis1	splicing factor Bis1
371	SPCC364.06	nap1	histone H2A-H2B chaperone Nap1
372	SPCC417.07c	mto1	gamma tubulin complex linker Mto1
373	SPCC417.09c		transcription factor (predicted)
374	SPCC4B3.12	set9	histone lysine H4-K20 methyltransferase Set9
375	SPCC4G3.15c	not2	CCR4-Not complex NOT box subunit Not2
376	SPCC4G3.19	alp16	gamma tubulin complex subunit Alp16
377	SPCC548.05c	dbl5	ubiquitin-protein ligase E3 Dbl5
378	SPCC550.12	arp6	actin-like protein Arp6
379	SPCC550.15c	rei1	ribosome biogenesis protein Rei1 (predicted)
380	SPCC553.04	cyp9	WD repeat containing cyclophilin family peptidyl-prolyl cis-trans isomerase Cyp9 (predicted)
381	SPCC576.13	swc5	Swr1 complex subunit Swc5
382	SPCC594.05c	spf1	Set1C ubiquitin-protein ligase E3 subunit Spf1
383	SPCC61.02	spt3	SAGA complex subunit Spt3
384	SPCC613.12c	raf1	CLRC ubiquitin ligase complex WD repeat subunit Raf1/Dos1
385	SPCC622.15c		Schizosaccharomyces specific protein
386	SPCC622.16c	epe1	Jmjc domain chromatin associated protein Epe1
387	SPCC622.19	jmj4	peptidyl-lysine 3-dioxygenase activity jmj4 (predicted)
388	SPCC645.13	bye1	transcription elongation regulator Bye1 (predicted)
389	SPCC663.11	saf1	splicing associated factor Saf1
390	SPCC663.12	cid12	poly(A) polymerase Cid12
391	SPCC736.08	cbf11	CBF1/Su(H)/LAG-1 family transcription factor Cbf11
392	SPCC736.11	ago1	argonaute
393	SPCC757.09c	rnc1	KH domain RNA-binding protein Rnc1
394	SPCC895.06	elp2	elongator complex WD repeat protein Elp2 (predicted)
395	SPCC895.07	alp14	TOG/XMAP215 microtubule plus end tracking polymerase Alp14
396	SPCC970.07c	raf2	CLRC ubiquitin ligase complex subunit Raf2

Table 2: Strain table

Strain	Genotype
PAS075	Locus2*::ade6p::3xE2C:hygMX* at Locus2 (between SPBC1711.11 and SPBC1711.12)
PM003	Wild-type strain: h(+); ura4-D18; leu1-32; ade6-M216; his7-366
PM006	972 h- wild-type
PAS193	Δ*K*::*ade6p:*mKO2; *ade6p:*SF-GFP between *REIII* and mat3M; *ade6p*:3xE2C*: hygMX* at Locus2; *clr4::kanMX,* h(-)
PAS216	*cenH*::*ade6p:*SF-GFP(Kint2); *mat3m(Eco*RV):: *ade6p:*mKO2; *ade6p:*3xE2C: *hygMX* at Locus2; *clr4::kanMX,* h90
PAS217	*cenH*: *ade6p:*SF-GFP (Kint2); *mat3m(Eco*RV):: *ade6p:*mKO2; *ade6p:*3xE2C: *hygMX* at Locus2, h90
PAS231	*ura4::natMX:dh:ade6p:*SF-GFP, *ade6p:*mKO2 3 kb, *leu1*::*ade6p:*3xE2C: *hygMX*
PAS331	*cenH*:: *ade6p:*SF-GFP (Kint2); *mat3m(Eco*RV):: *ade6p:*mKO2; *ade6p:*3xE2C:*hygMX* at Locus2; Δ*REIII*::REIII(Δs1, Δs2) in *clr4::kanMX,* h90
PAS332	*cenH*:: *ade6p:*SF-GFP (Kint2); *mat3m(Eco*RV):: *ade6p:*mKO2; *ade6p:*3xE2C:*hygMX* at Locus2; Δ*REIII*::REIII(Δs1, Δs2), h90
PAS482	Δ*K*::*ade6p:*mKO2; *ade6p:* SF-GFP between *REIII* and mat3M; *ade6p:*3xE2C*: hygMX* at Locus2, h(-); 'OFF' allele
PAS795	*cenH*: *ade6p:*SF-GFP (Kint2); *mat3m(Eco*RV):: *ade6p:*mKO2; *ade6p:*3xE2C: *hygMX* at Locus2; *fkh2::natMX*
PAS796	*cenH*: *ade6p:*SF-GFP (Kint2); *mat3m(Eco*RV):: *ade6p:*mKO2; *ade6p:*3xE2C: *hygMX* at Locus2; *prw1::kanMX*
PAS797	*cenH*: *ade6p:*SF-GFP (Kint2); *mat3m(Eco*RV):: *ade6p:*mKO2; *ade6p:*3xE2C: *hygMX* at Locus2; *png3::kanMX*
PAS798	*cenH*:: *ade6p:*SF-GFP (Kint2); *mat3m(Eco*RV):: *ade6p:*mKO2; *ade6p:*3xE2C:*hygMX* at Locus2; Δ*REIII*::REIII(Δs1, Δs2); *fkh2::natMX*
PAS799	*cenH*:: *ade6p:*SF-GFP (Kint2); *mat3m(Eco*RV):: *ade6p:*mKO2; *ade6p:*3xE2C:*hygMX* at Locus2; Δ*REIII*::REIII(Δs1, Δs2); *prw1::kanMX*
PAS800	*cenH*:: *ade6p:*SF-GFP (Kint2); *mat3m(Eco*RV):: *ade6p:*mKO2; *ade6p:*3xE2C:*hygMX* at Locus2; Δ*REIII*::REIII(Δs1, Δs2); *png3::kanMX*
PAS803	Δ*K*::*ade6p:*mKO2; *ade6p:* SF-GFP between *REIII* and mat3M; *ade6p:*3xE2C*: hygMX* at Locus2; 'OFF' allele; *fkh2::natMX*
PAS804	Δ*K*::*ade6p:*mKO2; *ade6p:* SF-GFP between *REIII* and mat3M; *ade6p:*3xE2C*: hygMX* at Locus2; 'OFF' allele; *prw1::kanMX*
PAS805	Δ*K*::*ade6p:*mKO2; *ade6p:* SF-GFP between *REIII* and mat3M; *ade6p:*3xE2C*: hygMX* at Locus2; 'OFF' allele; *png3::kanMX*
PAS808	*cenH*: *ade6p:*SF-GFP (Kint2); *mat3m(Eco*RV):: *ade6p:*mKO2; *ade6p:*3xE2C: *hygMX* at Locus2; *fkh2::natMX; prw1::kanMX* by cross
PAS809	*cenH*: *ade6p:*SF-GFP (Kint2); *mat3m(Eco*RV):: *ade6p:*mKO2; *ade6p:*3xE2C: *hygMX* at Locus2; *fkh2::natMX; prw1::kanMX* by sequential knockout
PAS810	*cenH*:: *ade6p:*SF-GFP (Kint2); *mat3m(Eco*RV):: *ade6p:*mKO2; *ade6p:*3xE2C:*hygMX* at Locus2; Δ*REIII*::REIII(Δs1, Δs2); *fkh2::natMX; prw1::kanMX* by cross
PAS811	*cenH*:: *ade6p:*SF-GFP (Kint2); *mat3m(Eco*RV):: *ade6p:*mKO2; *ade6p:*3xE2C:*hygMX* at Locus2; Δ*REIII*::REIII(Δs1, Δs2); *fkh2::natMX; prw1::kanMX* by sequential knockout
PAS813	*cenH*:: *ade6p:*SF-GFP (Kint2); *mat3m(Eco*RV):: *ade6p:*mKO2; *ade6p:*3xE2C:*hygMX* at Locus2; Δ*REIII*::REIII(Δs1, Δs2); *apm3::natMX*
PAS816	apl5:SF-GFP:*hygMX*; Swi6:E2C:*kanMX*
PAS817	apm3:SF-GFP:*hygMX;* Swi6:E2C:*kanMX*